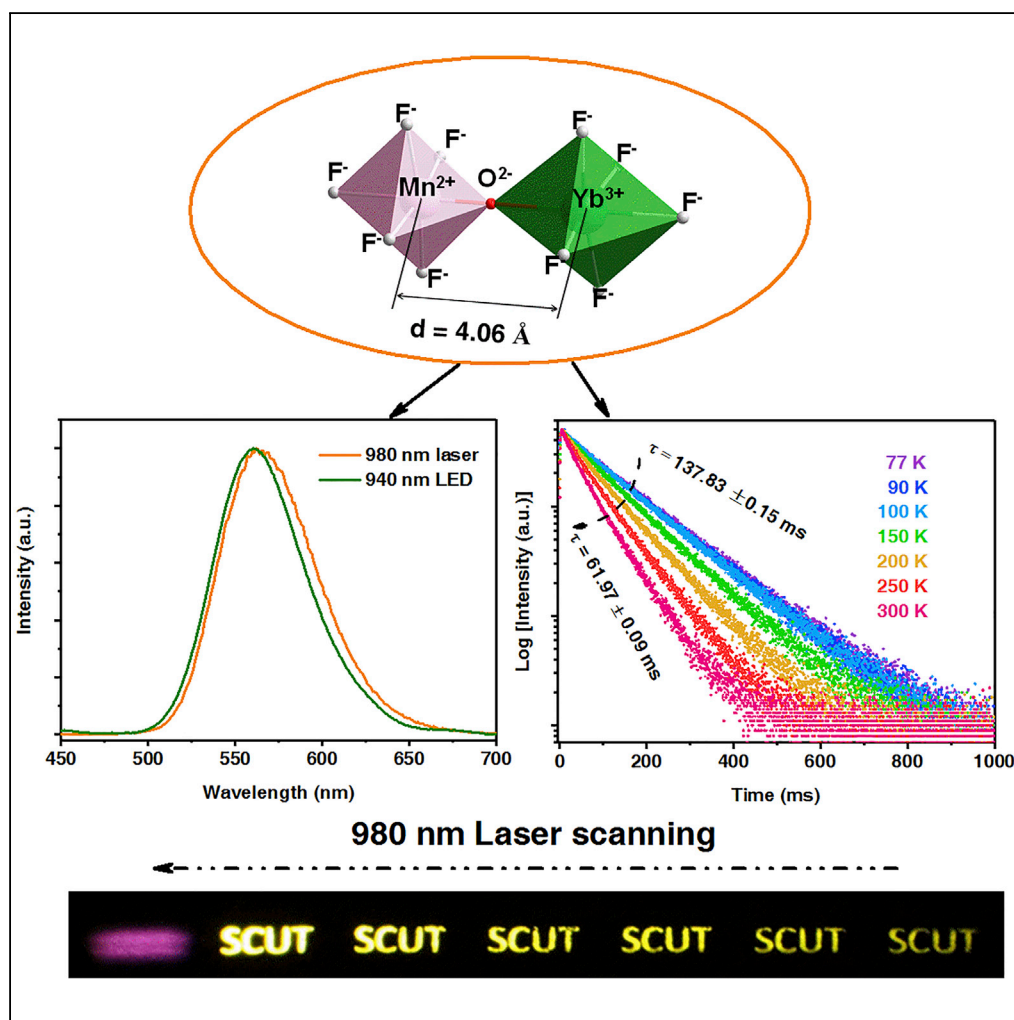


## Article

# Long-lived Photon Upconversion Phosphorescence in $\text{RbCaF}_3:\text{Mn}^{2+}, \text{Yb}^{3+}$ and the Dynamic Color Separation Effect



Enhai Song, Xinxin Han, Yayun Zhou, ..., Bo Zhou, Zhiguo Xia, Qinyuan Zhang

qyzhang@scut.edu.cn

## HIGHLIGHTS

Photon upconversion phosphorescence material  $\text{RbCaF}_3:\text{Mn}^{2+}, \text{Yb}^{3+}$  is developed

The UC emission center in  $\text{RbCaF}_3:\text{Mn}^{2+}, \text{Yb}^{3+}$  is ascribed to the  $\text{Yb}^{3+}-\text{Mn}^{2+}$  pair

A multiple anti-counterfeiting prototype based on the  $\text{RbCaF}_3:\text{Mn}^{2+}, \text{Yb}^{3+}$  is demonstrated

Song et al., iScience 19, 597–606  
 September 27, 2019 © 2019  
 The Author(s).  
<https://doi.org/10.1016/j.isci.2019.08.013>

## Article

# Long-lived Photon Upconversion Phosphorescence in $\text{RbCaF}_3:\text{Mn}^{2+}, \text{Yb}^{3+}$ and the Dynamic Color Separation Effect

Enhai Song,<sup>1</sup> Xinxin Han,<sup>1</sup> Yayun Zhou,<sup>1</sup> Yu Wei,<sup>1</sup> Xiao-Fang Jiang,<sup>1</sup> Shi Ye,<sup>1</sup> Bo Zhou,<sup>1</sup> Zhiguo Xia,<sup>1</sup> and Qinyuan Zhang<sup>1,2,\*</sup>

## SUMMARY

The development of luminescence materials with long-lived upconversion (UC) phosphorescence and long luminescence rise edge (LRE) is a great challenge to advance the technology of photonics and materials sciences. The lanthanide ions-doped UC materials normally possess limited UC lifetime and short LRE, restricting direct afterglow viewing in visual images by the naked eye. Here, we show that the  $\text{RbCaF}_3:\text{Mn}^{2+}, \text{Yb}^{3+}$  UC luminescence material generates a long UC lifetime of  $\sim 62$  ms peaking at 565 nm and an ultralong LRE of  $\sim 5.2$  ms. Density functional theory calculations provide a theoretical understanding of the  $\text{Mn}^{2+}\text{-Yb}^{3+}$  aggregation in the high-symmetry  $\text{RbCaF}_3$  host lattice that enables the formation of the long-lived UC emission center, superexchange coupled  $\text{Yb}^{3+}\text{-Mn}^{2+}$  pair. Through screen printing ink containing  $\text{RbCaF}_3:\text{Mn}^{2+}, \text{Yb}^{3+}$ , the visualized multiple anti-counterfeiting application and information encryption prototype with high-throughput rate of authentication and decryption are demonstrated by the dynamic color separation effect.

## INTRODUCTION

Luminescent materials with long-lived emission have been extensively investigated over the past decades and attracted increasing attention owing to their fundamental scientific importance and emerging applications, ranging from optoelectronics, bio-imaging, emergency signage, information encryption/decryption, and anti-counterfeiting (Pan et al., 2012; Maldiney et al., 2014; Li et al., 2016; Liu et al., 2017a, 2017b). Using the long-lived luminescent materials in information security, the persistent emission may be adopted for encryption, substantially increasing the difficulty of duplication or decryption and thus providing extra high-level security protection (Zhang et al., 2018; Zhuang et al., 2018; Liu et al., 2018). The conventional inorganic persistent emission materials yield afterglow emission of tens of hours, but they exhibit clear limitations of (1) the long pre-irradiation time to store the energy and (2) the UV or visible light excitation source enabling the inevitable background fluorescence in photoluminescence mode (Li et al., 2016; Wang et al., 2017; Matsuzawa et al., 1996). Therefore, the development of inorganic photon upconverting materials with minimum background interference that demonstrate afterglow emission without long-time pre-irradiation is crucial not only for fundamental research, but also for practical applications (Chen et al., 2018; Dong et al., 2017; Zhou et al., 2015; Gargas et al., 2014). However, the lifetimes of the conventional lanthanide ions doped upconversion (UC) luminescent materials are usually in the range of only several tens of microseconds to a few milliseconds (Auzel, 2004; Liu et al., 2017a, 2017b; Martín-Rodríguez et al., 2013), which does not meet the application requirements for direct viewing in visual images.

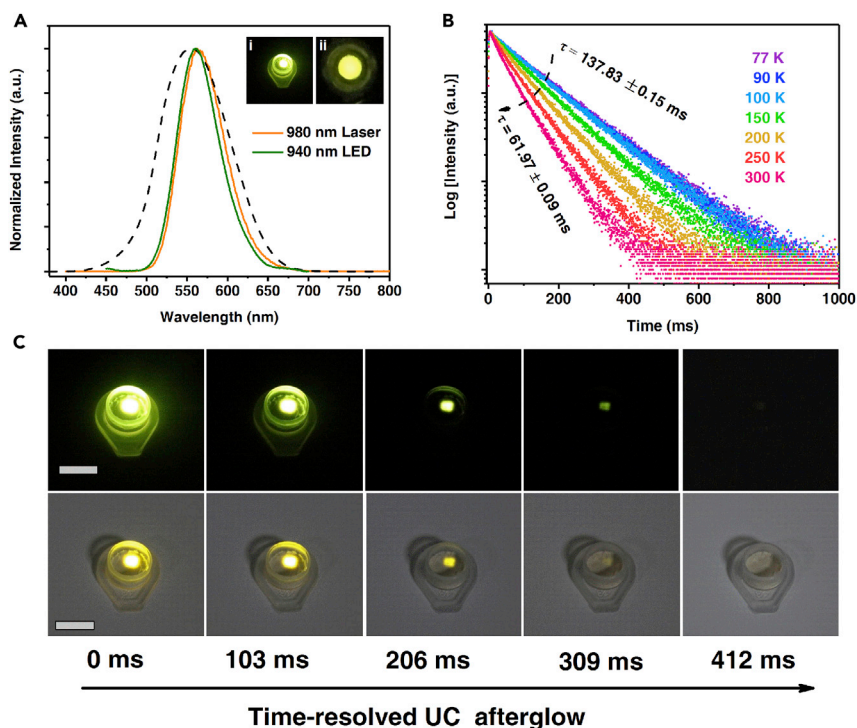
In contrast to the relatively short-lived emission of the lanthanide ions, the transition metal  $\text{Mn}^{2+}$  normally presents a long lifetime on the order of tens of milliseconds, originated from an inherent parity and spin double forbidden  $d-d$  transition [ ${}^4\text{T}_1({}^4\text{G}) \rightarrow {}^6\text{A}_1({}^6\text{S})$ ] (Feldmann et al., 2003; Yu et al., 2013; Lin et al., 2014; Vink et al., 2001; Zhou et al., 2018). In addition, the emission of  $\text{Mn}^{2+}$  depends strongly on crystal-field environment so that the wavelength-tunable  $\text{Mn}^{2+}$  UC emission with a long emission lifetime has been obtained in some  $\text{Mn}^{2+}/\text{Yb}^{3+}$  codoped structures upon 980-nm laser excitation (Suyver et al., 2005; Song et al., 2016). Nevertheless, because of the serious thermal and concentration quenching effects (Valiente et al., 2000; Martín-Rodríguez et al., 2010), or the aggregation of  $\text{Mn}^{2+}$  ions (Song et al., 2015), the  $\text{Mn}^{2+}$  UC emission is relatively weak and the emission lifetime is usually limited to less than 50 ms. Besides, the UC emission of  $\text{Mn}^{2+}$  has also been realized by constructing core-shell structure  $\text{NaGdF}_4:\text{Yb}/\text{Tm}/\text{NaGdF}_4:\text{Mn}$  (Liu et al., 2017a, 2017b; Li et al., 2015). However, since the  $\text{Mn}^{2+}$  UC emission belongs to a five-photon energy

<sup>1</sup>State Key Laboratory of Luminescent Materials and Devices, Guangdong Provincial Key Laboratory of Fiber Materials and Applied Techniques, Institute of Optical Communication Materials, South China University of Technology, Guangzhou 510641, China

<sup>2</sup>Lead Contact

\*Correspondence: qyzhang@scut.edu.cn  
<https://doi.org/10.1016/j.isci.2019.08.013>





**Figure 1. UC Photoluminescence and Phosphorescence in Perovskite  $\text{RbCaF}_3: \text{Mn}^{2+}, \text{Yb}^{3+}$**

(A) UC emission spectra of  $\text{RCF}:0.10\text{Mn}^{2+}, 0.05\text{Yb}^{3+}$  upon excitation with a 980-nm laser or incoherent light of a 940-nm LED with the sensitivity curve of the human eye (dotted line) also given as a comparison. The inset shows the UC luminescence pictures of  $\text{RCF}:0.10\text{Mn}^{2+}, 0.05\text{Yb}^{3+}$  powder upon 980-nm laser excitation (i) and the lightened UC luminescence LED fabricated with a 940-nm LED chip and  $\text{RCF}:0.10\text{Mn}^{2+}, 0.05\text{Yb}^{3+}$  powder (ii). (B) Temperature dependence of the UC luminescence decay curves of  $\text{RCF}:0.10\text{Mn}^{2+}, 0.05\text{Yb}^{3+}$  between 77 and 300 K. (C) Steady UC luminescence (0 ms) of  $\text{RCF}:0.10\text{Mn}^{2+}, 0.05\text{Yb}^{3+}$  and the time-resolved UC afterglow after stoppage of the laser under dark and daylight environment. (The images are recorded by a digital camera with an exposure time of 1/25 s using the snapshot mode.) The scale bar is 1 cm.

migration UC process in this system, the  $\text{Mn}^{2+}$  UC emission is much lower than that of the  $\text{Tm}^{3+}$  and the pure  $\text{Mn}^{2+}$  UC emission cannot be achieved, suggesting the limited applications.

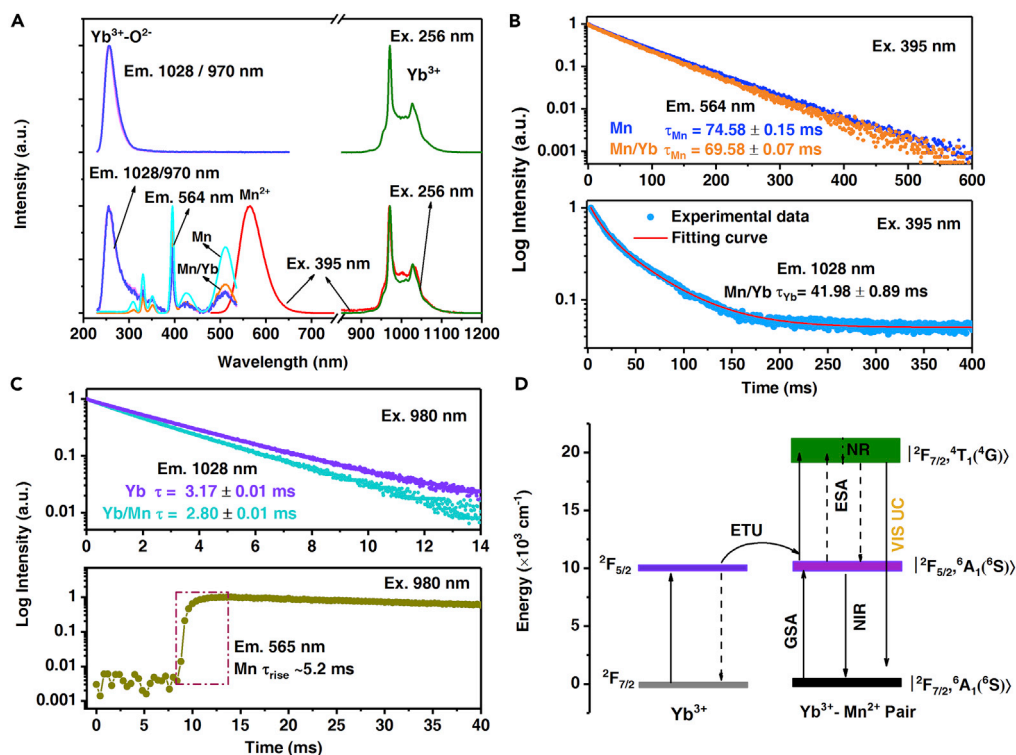
In the present study, to design an ideal system fulfilling the applications, the  $\text{Mn}^{2+}$ - $\text{Yb}^{3+}$  ions are introduced into the highly symmetric fluoride perovskite  $\text{RbCaF}_3$ , in which the  $\text{Mn}^{2+}$  and  $\text{Yb}^{3+}$  tend to aggregate, enabling the formation of a UC emission center, viz., superexchange coupled  $\text{Yb}^{3+}$ - $\text{Mn}^{2+}$  pair. Accordingly, an intense  $\text{Mn}^{2+}$ -based UC luminescence with a long emission lifetime of  $\sim 62$  ms has been achieved. Moreover, such a local structure forms an ultralong UC luminescence rise edge of  $\sim 5.2$  ms due to the energy transfer from the isolated  $\text{Yb}^{3+}$  ion to the exchange coupled  $\text{Yb}^{3+}$ - $\text{Mn}^{2+}$  pair. As the UC luminescence rise time and UC lifetime of the  $\text{RbCaF}:\text{Mn}^{2+}, \text{Yb}^{3+}$  are one to two orders of magnitude of conventional  $\text{Yb}^{3+}/\text{Er}^{3+}$  (or  $\text{Tm}^{3+}$ , or  $\text{Ho}^{3+}$ ) codoped UC materials, both of them have been applied into information encryption and high-level anti-counterfeiting based on the dynamic color separation effect. By using the UC luminescence material  $\text{RbCaF}:\text{Mn}^{2+}, \text{Yb}^{3+}$  to fabricate the screen printing ink, and comparing this ink with the ink containing commercialized UC red/green/blue (RGB) materials, the printing of images with multiple information encryption and a high level anti-counterfeiting application with a fast authentication rate have been demonstrated.

## RESULTS AND DISCUSSION

The UC materials  $\text{RbCa}_{1-x-y}\text{F}_3:\text{xMn}^{2+}, \text{yYb}^{3+}$  ( $0 < x \leq 0.20$ ;  $0 < y \leq 0.05$ ) (denoted as  $\text{RCF}:\text{xMn}^{2+}, \text{yYb}^{3+}$ ) have been prepared (see details on the phase structure and morphology characterizations in Figure S1) and the  $\text{RCF}:0.10\text{Mn}^{2+}, 0.05\text{Yb}^{3+}$  was selected as an example to study the UC luminescence and UC phosphorescence. Figure 1A presents the room temperature UC spectrum of  $\text{RCF}:0.10\text{Mn}^{2+}, 0.05\text{Yb}^{3+}$ . Upon

980-nm laser excitation, the sample exhibits an intense near-infrared to yellow UC emission, and the emission spectrum consists of a broadband emission peaking at 565 nm, corresponding to the  $d-d$  transition [ ${}^4T_1({}^4G) \rightarrow {}^6A_1({}^6S)$ ] of  $Mn^{2+}$ . The concentration-dependent UC emissions of RCF: $xMn^{2+}, yYb^{3+}$  ( $x = 0.10-0.30$ ;  $y = 0.05$ ) show that all samples contain a visible single-band UC emission, and the optimal doping concentration of  $Mn^{2+}$  is determined to be  $x = 0.10$  (see Figure S2A). The color purity of the material RCF:0.10 $Mn^{2+}, 0.05Yb^{3+}$  estimated from the spectrum was determined as  $\sim 98\%$ , showing much higher value than that of the conventional lanthanide-doped commercial UC emission materials (Figure S3). Moreover, such a pure yellow UC emission band is quite close to the highest sensitivity light region of the human eye (Vos, 1978), which is beneficial for the direct visual images as discussed later. On the other hand, the laser pumping is usually required to achieve UC luminescence (Zhong et al., 2015). Interestingly, the yellow UC emission of RCF: $Mn^{2+}, Yb^{3+}$  can be obtained even upon incoherent light excitation of a 940-nm light-emitting diode (LED) (Figure 1A). Additionally, the corresponding UC emission spectrum is almost completely overlapped with the spectrum excited by a 980-nm laser, meaning that the  $Mn^{2+}-Yb^{3+}$ -related UC luminescence process and mechanism pumped by laser were also achieved with incoherent light excitation in this case. When the temperature was gradually decreased from 300 to 77 K, the emission peak positions shifted from 568 to 587 nm, whereas the emission intensity was increased to  $\sim 420\%$  (Figure S4), ascribed to the shrinking of host lattice and the decreased non-irradiative relaxation processes, respectively. Correspondingly, the UC emission lifetime of  $Mn^{2+}$  was increased from 62 ms at 300 K to 138 ms at 77 K (Figure 1B). Such long lifetime and single-exponential decay behavior of  $Mn^{2+}$  at the temperatures of 77–300 K (Figure S4) show that only one type of UC emission centers appeared in RCF: $Mn^{2+}, Yb^{3+}$ . It is worth noting that the UC emission lifetime in RCF: $Mn^{2+}, Yb^{3+}$  is much longer than that of the previous reported  $Mn^{2+}$ -related UC systems (see Table S1). The long UC emission lifetime in RCF: $Mn^{2+}, Yb^{3+}$  is ascribed to the combined effect from the high symmetry of host lattice  $RbCaF_3$  and the un-aggregation characteristics of  $Mn^{2+}$  even at a high  $Mn^{2+}$  concentration ( $x = 0.30$ ) in this structure, which has been further confirmed by the concentration-dependent single-band visible UC and Stokes emissions in RCF: $xMn^{2+}, 0.05Yb^{3+}$  ( $x = 0.01-0.30$ ) (Figure S2). This is significantly different from the other similar  $Mn^{2+}/Yb^{3+}$  codoped perovskites  $AXF_3$  ( $A = Cs, Rb, K$ ;  $X = Mg, Zn, Cd$ ), and in  $AXF_3:xMn^{2+}, 0.005Yb^{3+}$ , the  $Mn^{2+}$  ions would aggregate as the  $Mn^{2+}$  concentration rises to  $x = 0.20$  (Song et al., 2015). Since the  $Mn^{2+}$  UC emission is strong enough with a long (62–138 ms) lifetime, the UC afterglow was observed by the naked eye in RCF: $Mn^{2+}, Yb^{3+}$  after stoppage of the laser irradiation, as shown in Figure 1C. Specifically, the UC afterglow time observed by the naked eye is longer than 300 ms in the daylight environment, whereas it is even longer than 400 ms in the dark environment. Furthermore, unlike the conventional long afterglow materials depending on the traps and the pre-radiation time (Pan et al., 2012; Li et al., 2016), the UC afterglow time of RCF: $Mn^{2+}, Yb^{3+}$  is only related with the UC emission lifetime of  $Mn^{2+}$ , and thus the UC afterglow was observed by the naked eye even with a 980-nm laser dynamic scanning (Video S1).

The UC luminescence of RCF: $Mn^{2+}, Yb^{3+}$  cannot be ascribed to the resonance energy transfer as reported in the  $Yb^{3+}/Er^{3+}$  (or  $Ho^{3+}$ , or  $Tm^{3+}$ ) codoped systems owing to the characteristic excitation/emission spectra of  $Mn^{2+}$  and  $Yb^{3+}$ . Except for the above-mentioned energy transfer UC mechanism, the cooperative sensitization can also lead to the  $Yb^{3+}/Mn^{2+}$  UC emission. Under this condition, a cooperative luminescence emission band of  $Yb^{3+}$  centered at  $\sim 490$  nm would usually simultaneously appear in the UC emission spectrum. However, the cooperative luminescence of  $Yb^{3+}$  has not been observed either in RCF: $Yb^{3+}$  or RCF: $Mn^{2+}, Yb^{3+}$ . Additionally, the occurrence of cooperative sensitization usually needs a relative high power density of the pump laser, whereas the UC emission of  $Mn^{2+}$  is observed in this system even pumped by using a 940-nm LED (incoherent light) excitation (Figure 1A), indicating that the possibility of the cooperative sensitization mechanism for generating  $Mn^{2+}$ -UC emission is quite low. Moreover, without observation of the  $Eu^{3+}$  UC emission in RCF: $Yb^{3+}, Eu^{3+}$  (Figure S5), thus the cooperative sensitization UC mechanism is excluded in this system. Upon 256-nm excitation, the emission spectrum of RCF:0.05 $Yb^{3+}$  consists of two sharp emission peaks at 970/1028 nm, corresponding to the  ${}^2F_{5/2} \rightarrow {}^2F_{7/2}$  transition of  $Yb^{3+}$  (Figure 2A). By monitoring the emission wavelengths at 970 and 1,028 nm, a similar excitation band centered at  $\sim 256$  nm was obtained, which is ascribed to the  $Yb^{3+}-O^{2-}$  charge transfer band (CTB) (Meijer et al., 2010; Yang et al., 2018). For RCF:0.10 $Mn^{2+}, 0.05Yb^{3+}$ , under 395-nm excitation, the  $Yb^{3+}$  emission at 970/1,028 nm was also obtained in addition to the Stokes emission ( $\sim 564$  nm) of  $Mn^{2+}$ . Moreover, the excitation spectrum of  $Yb^{3+}$  contains both the typical excitation peaks (310, 331, 351, 395, 424, and 511 nm) of the  $d-d$  transition of  $Mn^{2+}$  and  $O^{2-}-Yb^{3+}$  CTB (256 nm) of  $Yb^{3+}$ , indicating that the energy transfer from  $Mn^{2+}$  to  $Yb^{3+}$  occurs in RCF:0.10 $Mn^{2+}, 0.05Yb^{3+}$ . This result was further confirmed by the fact that the



**Figure 2. Down Conversion Luminescence Properties and UC Luminescence Mechanism of RbCaF<sub>3</sub>:Mn<sup>2+</sup>, Yb<sup>3+</sup>**

(A) Room temperature emission and excitation spectra of RCF:0.10Mn<sup>2+</sup>, 0.05Yb<sup>3+</sup> (Mn/Yb) and RCF:0.05Yb<sup>3+</sup>, and the excitation spectrum of RCF:0.10Mn<sup>2+</sup> (Mn) is given for comparison.

(B) Luminescence decay curves of Mn<sup>2+</sup> in RCF:0.10Mn<sup>2+</sup> and RCF:0.10Mn<sup>2+</sup>, 0.05Yb<sup>3+</sup> and the luminescence decay curve of Yb<sup>3+</sup> in RCF:0.10Mn<sup>2+</sup>, 0.05Yb<sup>3+</sup> upon 395-nm excitation. The lifetime of Yb<sup>3+</sup> upon 395-nm excitation is determined by fitting the acquired data with a double exponential function.

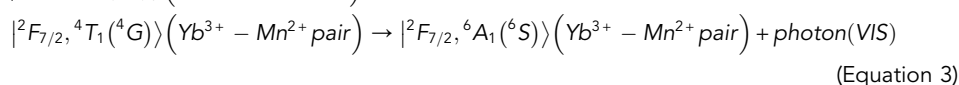
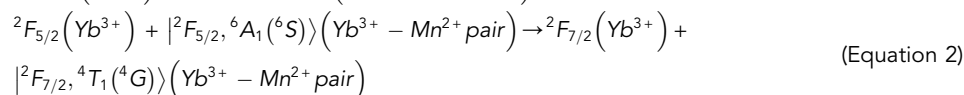
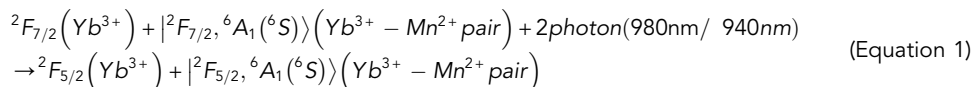
(C) Luminescence decay curves of Yb<sup>3+</sup> in RCF:0.05Yb<sup>3+</sup> and RCF:0.10Mn<sup>2+</sup>, 0.05Yb<sup>3+</sup> upon 980-nm laser excitation and the time-dependent UC luminescence of Mn<sup>2+</sup> between 0 and 40 ms.

(D) Ground state absorption (GSA)/energy transfer (ETU) UC luminescence mechanism based on isolated Yb<sup>3+</sup> ion and exchange coupled Yb<sup>3+</sup>-Mn<sup>2+</sup> pair.

emission intensity (Figure S6) and emission lifetime (Figure 2B) decrease in RbCF<sub>3</sub>:0.10Mn<sup>2+</sup>, 0.05Yb<sup>3+</sup> as compared with that of RbCF<sub>3</sub>:0.10Mn<sup>2+</sup>. Meanwhile, the excitation spectrum of Mn<sup>2+</sup> consists of the typical excitation peaks of the octahedral Mn<sup>2+</sup> only (Figure 2A). To give more information about the Mn<sup>2+</sup> UC emission, the luminescence decay curves of Yb<sup>3+</sup> (1,028 nm) in RCF:0.05Yb<sup>3+</sup> and RCF:0.10Mn<sup>2+</sup>, 0.05Yb<sup>3+</sup> were measured (see Figure 2C). It was found that the Mn<sup>2+</sup> codoping in RbCF<sub>3</sub>:Yb<sup>3+</sup> would cause the decrease of Yb<sup>3+</sup> lifetime, suggesting that the Mn<sup>2+</sup> UC emission in RCF:Mn<sup>2+</sup>, Yb<sup>3+</sup> resulted from the Yb<sup>3+</sup> → Mn<sup>2+</sup> energy transfer. However, the emission lines from Yb<sup>3+</sup> and the excitation spectrum of Mn<sup>2+</sup> have no spectral overlap. It is noted that the emission lifetime (~70 ms) of Mn<sup>2+</sup> in RCF:0.10Mn<sup>2+</sup>, 0.05Yb<sup>3+</sup> with 395-nm excitation is a little longer than that of UC emission lifetime (~62 ms) upon 980-nm laser excitation. Meanwhile, the emission lifetime value of Yb<sup>3+</sup> (1,028 nm, 42 ms) upon the characteristic excitation wavelength of Mn<sup>2+</sup> (395 nm) is much longer than that of 980-nm laser excitation (2.80 ms). Additionally, the Mn<sup>2+</sup> UC emission spectrum shifts to the longer wavelength region as compared with that of the Stokes emission (Figure S7); moreover, the Yb<sup>3+</sup> emission (970/1,028 nm) excited by 256-nm excitation shows some differences as compared with that by 395 nm excitation (Figure 2A). These facts strongly indicate that some types of new emission centers appeared in RCF:Mn<sup>2+</sup>, Yb<sup>3+</sup>. Furthermore, the UC emission of RCF<sub>3</sub>:0.10Mn<sup>2+</sup>, 0.05Yb<sup>3+</sup> upon 980-nm laser or 940-nm LED excitation belongs to a two-photon UC process (Figure S8) and a long UC luminescence rise time (~5.2 ms) was observed in this system (Figure 2C). Therefore, a possible UC luminescence mechanism based on isolated Yb<sup>3+</sup> ion and the exchange coupled Yb<sup>3+</sup>-Mn<sup>2+</sup> pair is proposed and is given in Figure 2D. Upon 980-nm laser or 940-nm LED excitation, both the isolated Yb<sup>3+</sup> and exchange coupled Yb<sup>3+</sup>-Mn<sup>2+</sup> pair are first excited to the state <sup>2</sup>F<sub>5/2</sub> of Yb<sup>3+</sup> and intermediate state |<sup>2</sup>F<sub>5/2</sub>, <sup>6</sup>A<sub>1</sub>(<sup>6</sup>S)) of the Yb<sup>3+</sup>-Mn<sup>2+</sup> pair, respectively. Then, the electron at the

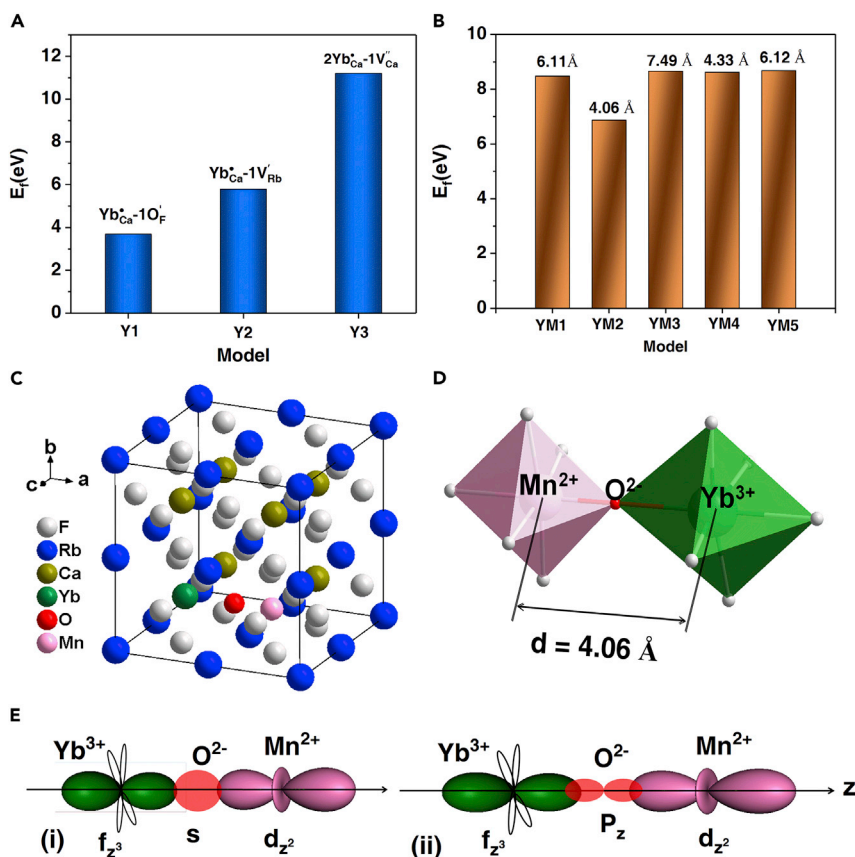


intermediate state  $|^2F_{5/2}, ^6A_1(^6S)\rangle$  is further excited to the emitting state  $|^2F_{7/2}, ^4T_1(^4G)\rangle$  ( $Yb^{3+}$ - $Mn^{2+}$  pair) through the energy transfer from isolated  $Yb^{3+}$  to  $Yb^{3+}$ - $Mn^{2+}$  pair and finally produces the visible (VIS) UC emission. The UC luminescence processes are provided as follows:



Different from the previously observed  $Mn^{2+}$  UC emissions in other systems (Valiente et al., 2001; Martín-Rodríguez et al., 2010; Gerner et al., 2004), the UC emission is mainly ascribed to a Ground state absorption (GSA)/ energy transfer (ETU) mechanism with the participation of both the  $Yb^{3+}$  ion and  $Yb^{3+}$ - $Mn^{2+}$  pair. The single-band UC emission characteristics and GSA/ETU UC mechanism of RCF: $Mn^{2+}$ , $Yb^{3+}$  indicate that the high-efficiency UC luminescence can be obtained via  $Mn^{2+}$ / $Yb^{3+}$  codoping (Suyver et al., 2005). Notably, the UC emission intensity of RCF: $Mn^{2+}$ , $Yb^{3+}$  is much stronger than that of the  $Mn^{2+}$ / $Yb^{3+}$  codoped similar perovskite fluorides  $AXF_3$  ( $A = Cs, Rb, K$ ;  $X = Mg, Zn, Cd$ ) (Figure S9). In addition, none of the  $AXF_3$ : $Mn^{2+}$ , $Yb^{3+}$  produces UC emission upon 940-nm LED excitation except for RCF: $Mn^{2+}$ , $Yb^{3+}$  found in this work. Therefore, the UC emission of RCF: $Mn^{2+}$ , $Yb^{3+}$  upon 940 nm LED excitation is mainly ascribed to the efficient UC emission (Table S2) and the obviously spectral overlap between the absorption of  $Yb^{3+}$  and the emission of the 940-nm LED (Figure S10).

On the basis of the comprehensive investigations of up and down-conversion luminescence in RCF: $Mn^{2+}$ , $Yb^{3+}$ , a superexchange coupled  $Yb^{3+}$ - $Mn^{2+}$  pair model has been proposed. During the formation of the  $Yb^{3+}$ - $Mn^{2+}$  pair, a critical distance of  $\sim 5$  Å between  $Mn^{2+}$  and  $Yb^{3+}$  was required (Valiente et al., 2000; Dexter, 1953). To evaluate the probability of formation of  $Yb^{3+}$ - $Mn^{2+}$  pair in RCF: $Mn^{2+}$ , $Yb^{3+}$ , the structure optimization based on density functional theory (DFT) was performed. The compound  $RbCaF_3$  presents a typical cubic perovskite structure with the  $Pm\bar{3}m$  space group (No. 221), consisting of a three-dimensional (3D) corner-sharing  $[CaF_6]$  octahedra network, where  $Rb^+$  ions are located at the centers of the tetrakaidecahedron cavity surrounded by  $[CaF_6]$  octahedron (see Figure S11). Considering the similar ionic radius and close valence states between  $Mn^{2+}$  (0.83 Å) and  $Ca^{2+}$  (1.0 Å), and between  $Yb^{3+}$  (0.87 Å) and  $Ca^{2+}$  (1.0 Å) (Shannon, 1976), both  $Mn^{2+}$  and  $Yb^{3+}$  would substitute for  $Ca^{2+}$  ion in RCF, accompanying the formation of Rb vacancy ( $V_{Rb}$ ) or Ca vacancy ( $V_{Ca}$ ) or introducing oxygen defect  $O_F'$  for charge compensation. Figure 3A presents that the formation energy ( $E_f$ ) for the different charge compensation models (Figure S12) of the  $Yb^{3+}$ -doped RCF. It is found that the  $E_f$  value for model Y1 shows much lower than others, suggesting that the substitution of  $Yb^{3+}$  for  $Ca^{2+}$  would generate one oxygen defect  $O_F'$  for charge compensation. Therefore, if both  $Ca^{2+}$  and  $Yb^{3+}$  are homogeneously distributed at the  $Ca^{2+}$  sites in RCF, the average distance between  $Mn^{2+}$  and  $Yb^{3+}$  is calculated as  $\sim 10.4$  Å in RCF:0.10 $Mn^{2+}$ ,0.05 $Yb^{3+}$  (Yang et al., 2005). This value is apparently much longer than that of the critical distance ( $\sim 5$  Å) for superexchange interactions, indicating that the formation probability of the  $Yb^{3+}$ - $Mn^{2+}$  pair would be relatively low in this structure, whereas the  $Mn^{2+}$  UC emission was observed even with a much lower concentration of  $Mn^{2+}$  and  $Yb^{3+}$  in RCF: $Mn^{2+}$ , $Yb^{3+}$  (Figure S13). Thus, the distributions of  $Mn^{2+}$  and  $Yb^{3+}$  in RCF: $Mn^{2+}$ , $Yb^{3+}$  were further simulated based on the site occupancy of  $Mn^{2+}$  and  $Yb^{3+}$  above. For a  $2 \times 2 \times 2$  supercell of RCF: $Mn^{2+}$ , $Yb^{3+}$ , $O^{2-}$ , there are five possible substitution models for  $Mn^{2+}$  (denoted as YM1-YM5, Figure S14). Figure 3B shows the  $E_f$  values of the five different substitution models, and the model YM2 exhibits the lowest  $E_f$  value, suggesting the model YM2 is the most stable model among them. Under this model, the nearest  $Yb^{3+}$ - $Mn^{2+}$  distance is of 4.06 Å (Figure 3C). Moreover, the distorted octahedron  $MnF_5O$  and distorted octahedron  $YbF_5O$  are connected with each other by sharing with one  $O^{2-}$  (Figure 3D); therefore, the superexchange coupled  $Yb^{3+}$ - $Mn^{2+}$  pair is formed in RCF: $Mn^{2+}$ , $Yb^{3+}$ . The linear  $Yb^{3+}$ - $O^{2-}$ - $Mn^{2+}$  configuration with a connected angle  $\angle Yb^{3+}$ - $O^{2-}$ - $Mn^{2+}$  of  $180^\circ$  would lead to a large overlap of the orbital wave-functions (Figure 3E) (Gerner et al., 2004). Meanwhile, the existence of oxygen of RCF: $Mn^{2+}$ , $Yb^{3+}$  was confirmed by the energy dispersive spectroscopy (Figure S15) and the X-ray photoelectron spectroscopy (Figure S16); moreover, the observation of  $Yb^{3+}$ - $O^{2-}$ -CTB also supports this model (Figure 2A). Hence, the UC luminescence of RCF: $Mn^{2+}$ , $Yb^{3+}$  is ascribed to



**Figure 3. Theoretical Simulation of the  $\text{Mn}^{2+}/\text{Yb}^{3+}$  Distribution in  $\text{RbCaF}_3:\text{Mn}^{2+},\text{Yb}^{3+}$**

(A) The formation energy ( $E_f$ ) for three possible charge compensation models (denoted as Y1, Y2, Y3) of  $\text{Yb}^{3+}$  in a  $2 \times 2 \times 2$  supercell of  $\text{RbCaF}_3:\text{Yb}^{3+}$ .

(B)  $E_f$  for five situations in a  $2 \times 2 \times 2$   $\text{RbCaF}_3:\text{Mn}^{2+},\text{Yb}^{3+},\text{O}^{2-}$  supercell with two  $\text{Ca}^{2+}$  ions substituted by one  $\text{Mn}^{2+}$  and one  $\text{Yb}^{3+}$  and one  $\text{F}^-$  replaced by one  $\text{O}^{2-}$  (denoted as YM1–YM5 with different shortest  $\text{Mn}^{2+}\text{-Yb}^{3+}$  distances after structure optimization).

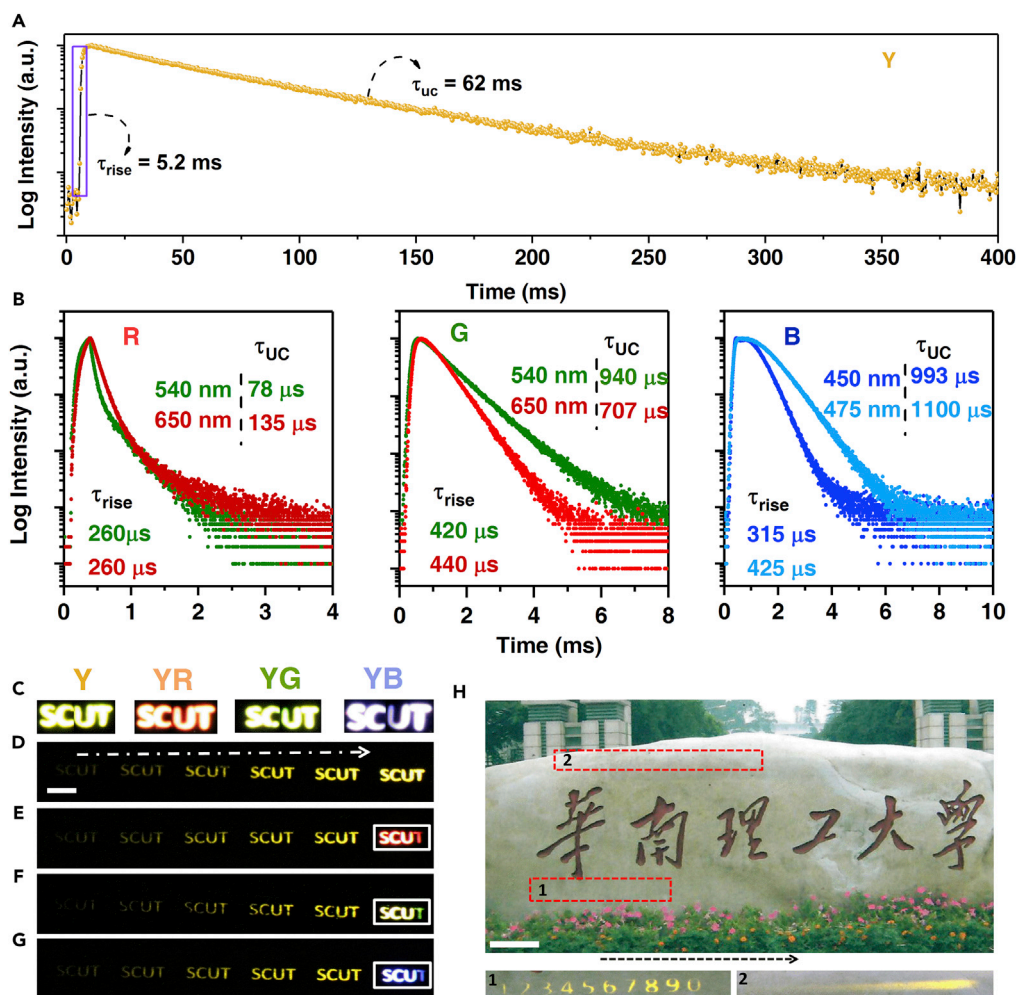
(C) Model YM1 after structure optimization.

(D) The  $\text{MnF}_5\text{O}$  and  $\text{YbF}_5\text{O}$  octahedron are connected by sharing with one  $\text{O}^{2-}$ .

(E) Schematic representation of the most important sigma overlaps between the  $d$  orbital of  $\text{Mn}^{2+}$  and  $f$  orbital of  $\text{Yb}^{3+}$  and the  $p(s)$  orbital of ligand  $\text{O}^{2-}$  with a bridging angle of  $180^\circ$ .

the  $|^2F_{7/2}, ^4T_1(^4G) \rightarrow |^2F_{7/2}, ^6A_1(^6S)$  transition of superexchange coupled  $\text{Yb}^{3+}\text{-Mn}^{2+}$  pair based on the energy transfer from the isolated  $\text{Yb}^{3+}$  ion to the  $\text{Yb}^{3+}\text{-Mn}^{2+}$  pair and the GSA process of the  $\text{Yb}^{3+}\text{-Mn}^{2+}$  pair. The UC emission lifetime (Figure S17) is a little shorter than the Stokes emission lifetime (Figure 2B) in  $\text{RCF:0.10Mn}^{2+},0.05\text{Yb}^{3+}$ , corresponding to the distorted crystal field environment for  $\text{Mn}^{2+}$  in the  $\text{Yb}^{3+}\text{-Mn}^{2+}$  pair (see Figure 3D and Table S3) and the additional increase in transition possibility due to the  $\text{Yb}^{3+}\text{-Mn}^{2+}$  interactions in the  $\text{Yb}^{3+}\text{-Mn}^{2+}$  pair (Martín-Rodríguez et al., 2010).

As both the luminescence rise edge and UC emission lifetime of  $\text{RCF:0.10Mn}^{2+},0.05\text{Yb}^{3+}$  (denoted as Y) are obviously longer than those of the commercial red  $\beta\text{-NaYF}_4:6\%\text{Er}^{3+}$  (denoted as R), green  $\beta\text{-NaYF}_4:20\%\text{Yb}^{3+},2\%\text{Er}^{3+}$  (denoted as G), and blue  $\beta\text{-NaYF}_4:18\%\text{Yb}^{3+},2\%\text{Tm}^{3+}$  (denoted as B) UC phosphors (Figures 4A and 4B), one can easily separate the two kinds of UC emissions based on the different dynamic color separation effect during the luminescence rise and decay stage, respectively. The unique color separation characteristics may find application in advanced multiple information encryption and the high-level anti-counterfeiting. As a proof of concept, four types of security inks (Y, YR, YG, and YB) (see detail in Table S4) were designed and fabricated by using the as-prepared  $\text{RCF:0.10Mn}^{2+},0.05\text{Yb}^{3+}$ , the commercial R, G, and B UC materials. By using these security inks, the “SCUT” patterns were printed on the multipurpose paper via the screen-printing technique (Figure S18A). Figure 4C illustrates the luminescence images of the



**Figure 4. Multiple Information Encryption and Anti-counterfeiting Applications Based on the Long UC Lifetime and Ultralong Luminescence Rise Edge of  $\text{RbCaF}_3:\text{Mn}^{2+}, \text{Yb}^{3+}$**

(A) Room-temperature luminescence decay curve of  $\text{RbCaF}_3:\text{Mn}^{2+}, \text{Yb}^{3+}$ .

(B) UC luminescence decay curves of commercial red (R), green (G), and blue (B) UC phosphors upon 980-nm laser

excitation. Here, the UC emission lifetime is determined by  $\tau_{\text{uc}} = \frac{1}{I_0} \int_0^{\infty} I(t) dt$ , where  $I_0$  and  $I(t)$  are the maximum emission intensity and the emission intensity at time  $t$  after cutoff the pump laser, respectively.

(C–G) Luminescence images of the "SCUT" pattern printed by inks Y, YR, YG, YB with a 980-nm laser steady excitation (C) or dynamic scanning (D–F correspond to inks Y, YR, YG and YB, respectively).

(H) Using ink Y to print some designed patterns in different areas (1, pattern "1234567890"; 2, pattern "strip") of a Chinese postcard and the luminescence images under 980-nm laser dynamic scanning. The scale bar is 10 mm. The dynamic luminescence photographs were recorded using a digital camera with an exposure time step of 1/50s. The power density and spot diameter of the used 980-nm laser are 10  $\text{W}/\text{cm}^2$  and 3.0 mm, respectively.

patterns upon steady 980-nm laser (29.59  $\text{W}/\text{cm}^2$ ) excitation in a dark environment. It was observed that the "SCUT" patterns printed by Y, YR, YG, and YB inks show intense yellow, orange, yellow-green, and white emission, respectively, matching well with their steady UC emission spectra (Figure S19). The emission color of the "SCUT" patterns can be further tuned by varying the pump power density of the laser (Figure S20 and Table S5). Interestingly, after using a 980-nm laser fast scanning the "SCUT" pattern printed by ink Y, six yellow luminescence "SCUT" patterns were unambiguously observed (see Figure 4D and Video S2), and a similar phenomenon has been also obtained under a daylight environment condition (Figure S21A and Video S3). Furthermore, one can observe the pattern "SCUT" afterglow even with a relative low-power-density ( $\sim 2.72 \text{ W}/\text{cm}^2$ ) laser fast scanning (Figure S21B). For other inks, upon irradiation with a 980-nm laser dynamic scanning, the letters highlighted with white border show different emitting colors, but five



identical yellow UC afterglow “SCUT” patterns can be observed (see [Figures 4E–4G](#) and the [Videos S4, S5, and S6](#)). Moreover, in the “SCUT” pattern upon 980-nm laser dynamic irradiation, the letter “T” showed red for YR ink, green for YG ink, and blue for YB, whereas the corresponding “SCU” exhibited orange, yellow-green, and white emissions, respectively. This is because the luminescence rise edge of RCF:Mn<sup>2+</sup>,Yb<sup>3+</sup> is significantly longer than that of commercial UC materials and the latter could achieve their steady state more rapidly than the former, which is further validated by the time-resolved UC emission ([Figure S19](#)) and the pulse-widths dependence of the UC emissions ([Figure S22](#)). These results demonstrate that both the long UC luminescence rise and long UC lifetime of RCF:Mn<sup>2+</sup>,Yb<sup>3+</sup> can be applied in information encryption and show fast decryption characteristics. The information of RCF:Mn<sup>2+</sup>,Yb<sup>3+</sup> and the commercial UC phosphors can be fast distinguished in observing windows II and I, respectively, through the dynamic color separation effect.

Additionally, the potential anti-counterfeiting application using the RCF:Mn<sup>2+</sup>,Yb<sup>3+</sup> phosphor was also demonstrated. As shown in [Figure 4H](#), the patterns of “1234567890” and “strip” were printed on 1 and 2 areas of a Chinese postcard. After drying, it is difficult to recognize the colorless patterns using the naked eye under daylight conditions. However, after using a 980-nm laser fast scanning, yellow afterglow “1234567890” and tailed emission in yellow were observed by the naked eye in areas 1 and 2, respectively. These observations revealed that RCF:Mn<sup>2+</sup>,Yb<sup>3+</sup> material provided a high level anti-counterfeiting application with a fast authentication rate. In addition, the authentication will not be affected by the ambient light.

### Conclusion

In summary, we have successfully developed an upconverting RCF:Mn<sup>2+</sup>,Yb<sup>3+</sup> material with a long (~62–138 ms) lifetime and long luminescence rise edge (~5.2 ms). One can observe UC afterglow by the naked eye upon 980-nm fast irradiation even under daylight environment with a significant visualized UC afterglow >300 ms. The long-lived UC emission is ascribed to the  $|^2F_{7/2}, ^4T_1(^4G)\rangle \rightarrow |^2F_{7/2}, ^6A_1(^6S)\rangle$  transition of superexchange coupled Yb<sup>3+</sup>-Mn<sup>2+</sup> pair formed in RCF:Mn<sup>2+</sup>,Yb<sup>3+</sup>. The long UC luminescence rise edge is originated from the energy transfer from the isolated Yb<sup>3+</sup> to Yb<sup>3+</sup>-Mn<sup>2+</sup> pair. The DFT calculations and spectra analysis verify that the UC emission is attributed to the formation of linear {Yb<sup>3+</sup>-O<sup>2-</sup>-Mn<sup>2+</sup>} unit in RCF:Mn<sup>2+</sup>,Yb<sup>3+</sup>. Given the single-band emission characteristics and two-photon GSA/ETU energy transfer UC mechanism, the highly efficient UC luminescence can be realized through Mn<sup>2+</sup>/Yb<sup>3+</sup> codoping.

On the basis of the special characters of the ultralong UC luminescence rise edge and long UC emission lifetime of RCF:Mn<sup>2+</sup>,Yb<sup>3+</sup>, new types of visualized multiple information encryption and anti-counterfeiting with fast decryption rate were demonstrated. These findings show great promise of RCF:Mn<sup>2+</sup>,Yb<sup>3+</sup> for use in advanced anticounterfeiting and multiple information encryption applications without the need of time-gated setup to separate and decode security data and also provide new insights for the dynamic printing color separation and exploration of advanced photon materials.

### Limitations of the Study

The distribution of Mn<sup>2+</sup> is important for the UC emission intensity and UC lifetime of the RbCaF<sub>3</sub>:Mn<sup>2+</sup>,Yb<sup>3+</sup>. Further in-depth study about the effects of Mn<sup>2+</sup> distributions on the performance of the Mn<sup>2+</sup>/Yb<sup>3+</sup>-related UC materials should be carried out. In addition, the stability of the UC material RbCaF<sub>3</sub>:Mn<sup>2+</sup>/Yb<sup>3+</sup> has not been investigated and is worth investigating in the future, which is critical for the practical application.

### METHODS

All methods can be found in the accompanying [Transparent Methods supplemental file](#).

### SUPPLEMENTAL INFORMATION

Supplemental Information can be found online at <https://doi.org/10.1016/j.isci.2019.08.013>.

### ACKNOWLEDGMENTS

This research was financially supported by the National Science Foundation of China (Grant Nos. 51472088, 51602104, 51603069, and U1601205), Natural Science Foundation of Guangdong Province, China. (Grant No. 2016A030310432, 2017A030313287).

## AUTHOR CONTRIBUTIONS

E.S and Q.Z. conceived of the project and designed the experiments; X.H., Y.W., and X.-F.J. synthesized the materials and performed experimental characterization; E.S. and Y.Z. performed the security ink printing and imaging; E.S., S.Y., and B.Z. contributed the UC luminescence mechanism analysis; E.S. performed the DFT calculations and interpretation of the computational data; E.S., Z.X., and Q.Z. wrote the paper; all authors contributed to the data analyses.

## DECLARATION OF INTERESTS

The authors declare no competing interests.

Received: May 25, 2019

Revised: July 14, 2019

Accepted: August 5, 2019

Published: September 27, 2019

## REFERENCES

- Auzel, F. (2004). Upconversion and anti-stokes processes with f and d ions in solids. *Chem. Rev.* *104*, 139–174.
- Chen, S., Weitemier, A.Z., Zeng, X., He, L., Wang, X., Tao, Y., Huang, A.J.Y., Hashimoto, Y., Kano, M., Iwasaki, H., et al. (2018). Near-infrared deep brain stimulation via upconversion nanoparticle-mediated optogenetics. *Science* *359*, 679–684.
- Dexter, D.L. (1953). A theory of sensitized luminescence in solids. *J. Chem. Phys.* *21*, 836–850.
- Dong, H., Sun, L., Feng, W., Gu, Y., Li, F., and Yan, C. (2017). Versatile spectral and lifetime multiplexing nanoplatform with excitation orthogonalized upconversion luminescence. *ACS Nano* *11*, 3289–3297.
- Feldmann, C., Jüstel, T., Ronda, C.R., and Schmidt, P.J. (2003). Inorganic luminescent materials: 100 years of research and application. *Adv. Funct. Mater.* *13*, 511–516.
- Gargas, D.J., Chan, E.M., Ostrowski, A.D., Aloni, S., Altoe, M.V.P., Barnard, E.S., Sanii, B., Urban, J.J., Milliron, D.J., Cohen, B.E., et al. (2014). Engineering bright sub-10-nm upconverting nanocrystals for single-molecule imaging. *Nat. Nanotechnol.* *9*, 300–305.
- Gerner, P., Reinhard, C., and Güdel, H.U. (2004). Cooperative near-IR to visible photon upconversion in Yb<sup>3+</sup>-Doped MnCl<sub>2</sub> and MnBr<sub>2</sub>: comparison with a Series of Yb<sup>3+</sup>-Doped Mn<sup>2+</sup> halides. *Chem. Europ. J.* *10*, 4735–4741.
- Li, X., Liu, X., Chevrier, D.M., Qin, X., Xie, X., Song, S., Zhang, H., Zhang, P., and Liu, X. (2015). Energy migration upconversion in manganese(II)-doped nanoparticles. *Angew. Chem. Int. Ed.* *54*, 13312–13317.
- Li, Y., Gecevicius, M., and Qiu, J. (2016). Long persistent phosphors-from fundamentals to applications. *Chem. Soc. Rev.* *45*, 2090–2136.
- Lin, J., Zhang, Q., Wang, L., Liu, X., Yan, W., Wu, T., Bu, X., and Feng, P. (2014). Atomically precise doping of monomanganese ion into coreless supertetrahedral chalcogenide nanocluster inducing unusual red shift in Mn<sup>2+</sup> emission. *J. Am. Chem. Soc.* *136*, 4769–4779.
- Liu, J., Wang, N., Yu, Y., Yan, Y., Zhang, H., Li, J., and Yu, J. (2017a). Carbon dots in zeolites: a new class of thermally activated delayed fluorescence materials with ultralong lifetimes. *Sci. Adv.* *3*, e1603171.
- Liu, X., Wang, Y., Li, X., Yi, Z., Deng, R., Liang, L., Xie, X., Loong, D.T.B., Song, S., Fan, D., et al. (2017b). Binary temporal upconversion codes of Mn<sup>2+</sup>-activated nanoparticles for multilevel anti-counterfeiting. *Nat. Commun.* *8*, 899.
- Liu, Z., Zhao, L., Chen, W., Fan, X., Yang, X., Tian, S., Yu, X., Qiu, J., and Xu, X. (2018). Multiple anti-counterfeiting realized in NaBaScSi<sub>2</sub>O<sub>7</sub> with a single activator of Eu<sup>2+</sup>. *J. Mater. Chem. C* *6*, 11137–11143.
- Maldiney, T., Bessière, A., Seguin, J., Teston, E., Sharma, S.K., Viana, B., Bos, A.J.J., Dorenbos, P., Bessodes, M., Gourier, D., et al. (2014). The in vivo activation of persistent nanophosphors for optical imaging of vascularization, tumours and grafted cells. *Nat. Mater.* *13*, 418–426.
- Martín-Rodríguez, R., Fischer, S., Ivaturi, A., Froehlich, B., Krämer, K.W., Goldschmidt, J.C., Richards, B.S., and Meijerink, A. (2013). Highly efficient IR to NIR upconversion in Gd<sub>2</sub>O<sub>3</sub>: Er<sup>3+</sup> for photovoltaic applications. *Chem. Mater.* *25*, 1912–1921.
- Martín-Rodríguez, R., Valiente, R., Piccinelli, F., and Bettinelli, M. (2010). Temperature dependence and temporal dynamics of Mn<sup>2+</sup> upconversion luminescence sensitized by Yb<sup>3+</sup> in codoped LaMgAl<sub>11</sub>O<sub>19</sub>. *Phys. Rev. B* *82*, 75117.
- Matsuzawa, T., Aoki, Y., Takeuchi, N., and Murayama, Y. (1996). A new long phosphorescent phosphor with high brightness, SrAl<sub>2</sub>O<sub>4</sub>:Eu<sup>2+</sup>, Dy<sup>3+</sup>. *J. Electrochem. Soc.* *143*, 2670–2673.
- Meijer, J.M., Aarts, L., van der Ende, B.M., Vlugt, T.J.H., and Meijerink, A. (2010). Downconversion for solar cells in YF<sub>3</sub>:Nd<sup>3+</sup>, Yb<sup>3+</sup>. *Phys. Rev. B* *81*, 35107.
- Pan, Z., Lu, Y., and Liu, F. (2012). Sunlight-activated long-persistent luminescence in the near-infrared from Cr<sup>3+</sup>-doped zinc gallogermanates. *Nat. Mater.* *11*, 58–63.
- Shannon, R.T. (1976). Revised effective ionic radii and systematic studies of interatomic distances in halides and chalcogenides. *Acta Crystallogr.* *32*, 751–767.
- Song, E., Chen, Z., Wu, M., Ding, S., Ye, S., Zhou, S., and Zhang, Q. (2016). Room-temperature wavelength-tunable single band upconversion luminescence from Yb<sup>3+</sup>/Mn<sup>2+</sup> codoped fluoride perovskites ABF<sub>3</sub>. *Adv. Opt. Mater.* *4*, 798–806.
- Song, E., Ye, S., Liu, T., Du, P., Si, R., Jing, X., Ding, S., Peng, M., Zhang, Q., and Wondraczek, L. (2015). Tailored Near-infrared photoemission in fluoride perovskites through activator aggregation and super-exchange between divalent manganese ions. *Adv. Sci.* *2*, 1500089.
- Suyver, J.F., Aebischer, A., Biner, D., Gerner, P., Grimm, J., Heer, S., Krämer, K.W., Reinhard, C., and Güdel, H.U. (2005). Novel materials doped with trivalent lanthanides and transition metal ions showing near-infrared to visible photon upconversion. *Opt. Mater.* *27*, 1111–1130.
- Valiente, R., Wenger, O.S., and Güdel, H.U. (2000). New photon upconversion processes in Yb<sup>3+</sup> doped CsMnCl<sub>3</sub> and RbMnCl<sub>3</sub>. *Chem. Phys. Lett.* *320*, 639–644.
- Valiente, R., Wenger, O.S., and Güdel, H.U. (2001). Near-infrared-to-visible photon upconversion process induced by exchange interactions in Yb<sup>3+</sup>-doped RbMnCl<sub>3</sub>. *Phys. Rev. B* *63*, 165102.
- Vink, A.P., De Bruin, M.A., Roke, S., Peijzel, P.S., and Meijerink, A. (2001). Luminescence of exchange coupled pairs of transition metal ions. *J. Electrochem. Soc.* *148*, E313–E320.
- Vos, J.J. (1978). Colorimetric and photometric properties of a 2-deg fundamental observer. *Color Res. Appl.* *3*, 125–128.
- Wang, J., Ma, Q., Zheng, W., Liu, H., Yin, C., Wang, F., Chen, X., Yuan, Q., and Tan, W. (2017). One-dimensional luminous nanorods featuring tunable persistent luminescence for autofluorescence-free biosensing. *ACS Nano* *11*, 8185–8191.

Yang, W., Luo, L., Chen, T., and Wang, N. (2005). Luminescence and energy transfer of Eu- and Mn-coactivated  $\text{CaAl}_2\text{Si}_2\text{O}_8$  as a potential phosphor for white-light UVLED. *Chem. Mater.* *17*, 3883–3888.

Yang, Y., Li, Z., Zhang, J., Lu, Y., Guo, S., Zhao, Q., Wang, X., Yong, Z., Li, H., Ma, J., et al. (2018). X-ray-activated long persistent phosphors featuring strong UVC afterglow emissions. *Light Sci. Appl.* *7*, 88.

Yu, J.H., Kwon, S., Petrášek, Z., Park, O.K., Jun, S.W., Shin, K., Choi, M., Park, Y.I., Park, K., and Na, H.B. (2013). High-resolution three-photon biomedical imaging using doped ZnS nanocrystals. *Nat. Mater.* *12*, 359–366.

Zhang, J., Pan, C., Zhu, Y., Zhao, L., He, H., Liu, X., and Qiu, J. (2018). Achieving thermo-mechano-opto-responsive bitemporal colorful luminescence via multiplexing of dual lanthanides in piezoelectric particles and its multidimensional anticounterfeiting. *Adv. Mater.* *30*, 1804644.

Zhong, Y., Rostami, I., Wang, Z., Dai, H., and Hu, Z. (2015). Energy migration engineering of bright rare-earth upconversion nanoparticles for excitation by light-emitting diodes. *Adv. Mater.* *27*, 6418–6422.

Zhou, B., Shi, B., Jin, D., and Liu, X. (2015). Controlling upconversion nanocrystals for

emerging applications. *Nat. Nanotechnol.* *10*, 924–936.

Zhou, Q., Dolgov, L., Srivastava, A.M., Zhou, L., Wang, Z., Shi, J., Drami Anin, M.D., Brik, M.G., and Wu, M. (2018).  $\text{Mn}^{2+}$  and  $\text{Mn}^{4+}$  red phosphors: synthesis, luminescence and applications in WLEDs. A review. *J. Mater. Chem. C* *6*, 2652–2671.

Zhuang, Y., Wang, L., Lv, Y., Zhou, T., and Xie, R. (2018). Optical data storage and multicolor emission readout on flexible films using deep-trap persistent luminescence materials. *Adv. Funct. Mater.* *28*, 1705769.

**ISCI, Volume 19**

**Supplemental Information**

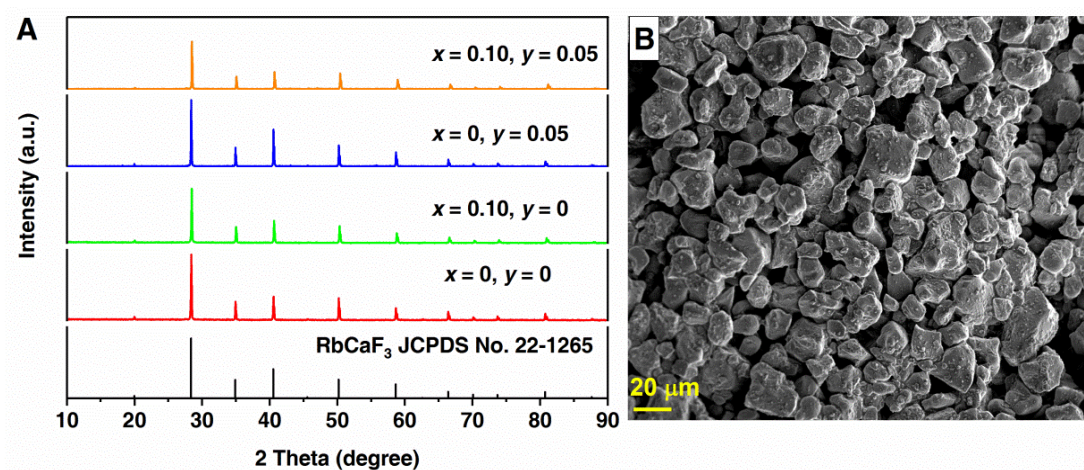
**Long-lived Photon Upconversion**

**Phosphorescence in  $\text{RbCaF}_3:\text{Mn}^{2+},\text{Yb}^{3+}$**

**and the Dynamic Color Separation Effect**

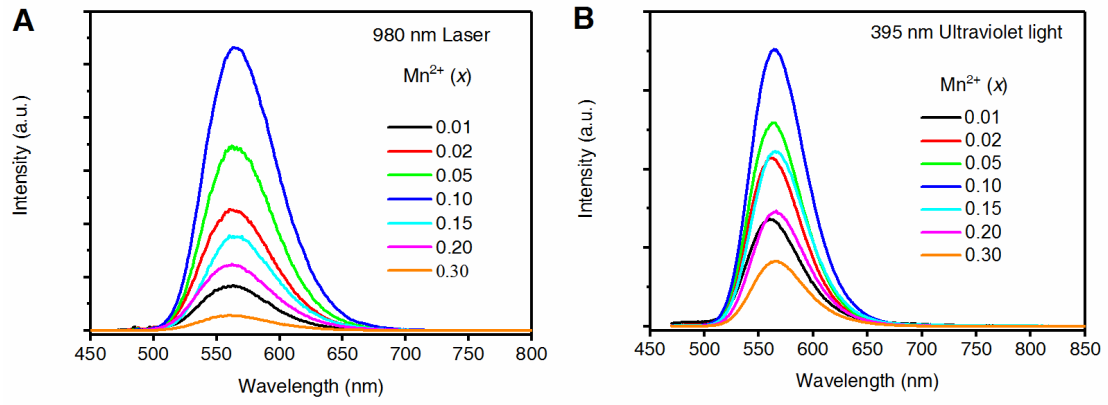
**Enhai Song, Xinxin Han, Yayun Zhou, Yu Wei, Xiao-Fang Jiang, Shi Ye, Bo Zhou, Zhiguo Xia, and Qinyuan Zhang**

## Supplemental Figures

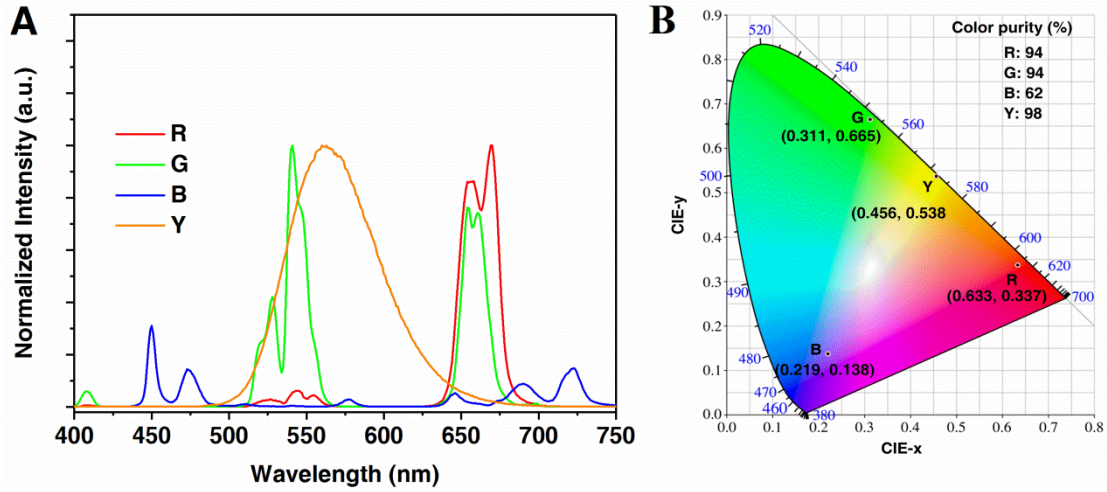


**Figure S1.** The XRD patterns and typical SEM of RbCaF<sub>3</sub>:Mn<sup>2+</sup>,Yb<sup>3+</sup>, related to Figure 1. (A) XRD patterns of RCF:*x*Mn<sup>2+</sup>,*y*Yb<sup>3+</sup> (*x* = 0, 0.10; *y* = 0, 0.05) and (B) SEM image of RCF:0.10Mn<sup>2+</sup>,0.05Yb<sup>3+</sup>.





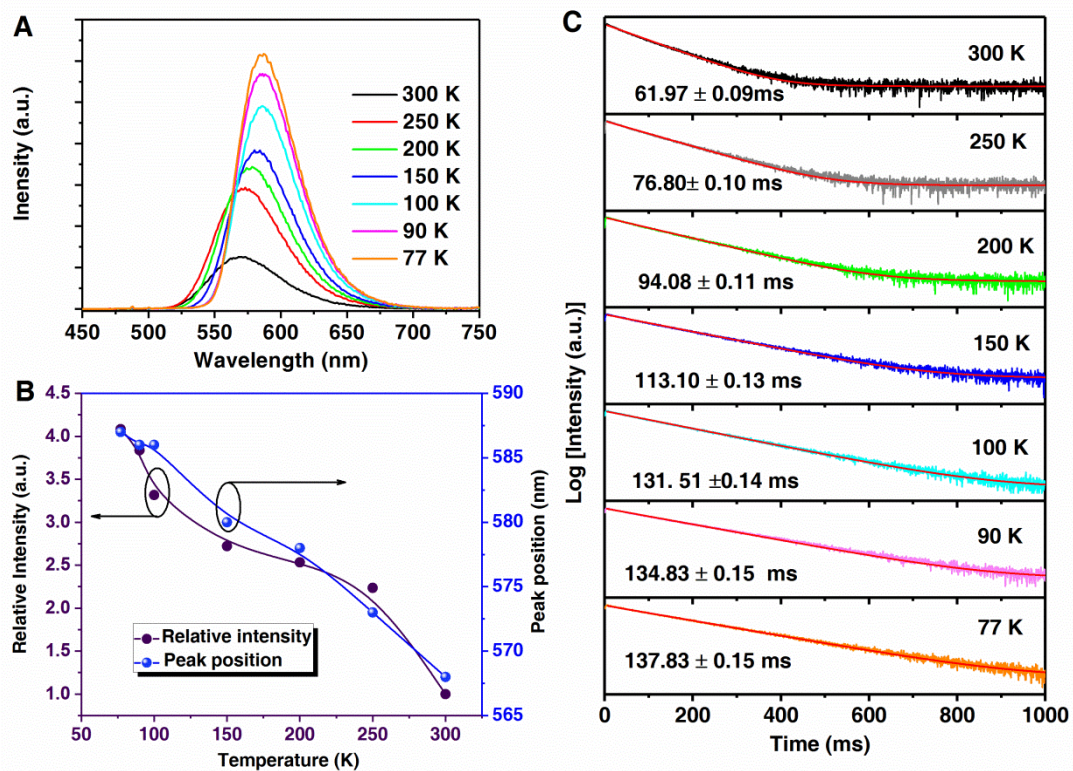
**Figure S2. Stokes and UC emission spectra of  $\text{RbCa}_{0.95}\text{F}_3:x\text{Mn}^{2+},0.05\text{Yb}^{3+}$ , related to Figure 1. (A) Stokes and (B) UC emission spectra of  $\text{RbCa}_{0.95}\text{F}_3:x\text{Mn}^{2+},0.05\text{Yb}^{3+}$  ( $x = 0.01-0.30$ ).**



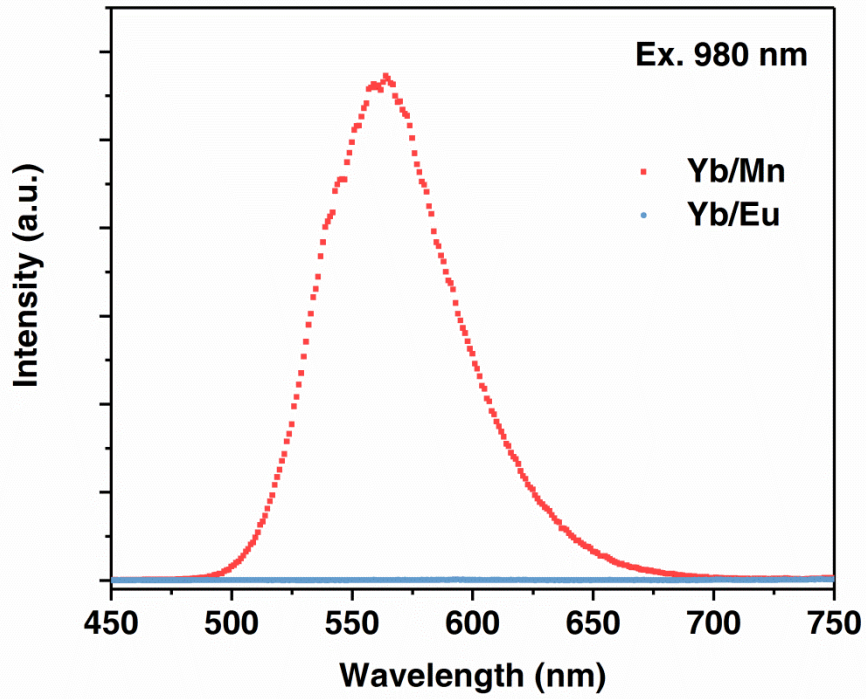
**Figure S3. UC emission spectra, colour purity and CIE coordinates of the conventional UC materials and  $\text{RCaF}_3:\text{Mn}^{2+}, \text{Yb}^{3+}$ , related to Figure 1. (A)** UC emission spectra of the commercial red (R), green (G) and blue UC phosphors, and as-synthesized yellow UC phosphor  $\text{RCF}:\text{0.10Mn}^{2+}, \text{0.05Yb}^{3+}$  (Y) under steady 980 nm laser excitation. **(B)** Chromaticity coordinates and color purity of the commercial RGB UC phosphors, and as-synthesized yellow phosphor  $\text{RCF}:\text{0.10Mn}^{2+}, \text{0.05Yb}^{3+}$  (Y) under the sample measure condition. Both commercial red and green UC phosphors are based on  $\text{Yb}^{3+}/\text{Er}^{3+}$  codoping, while the commercial blue UC phosphor is achieved through  $\text{Yb}^{3+}/\text{Tm}^{3+}$  codoping. For red and green UC phosphors, the emission peaks at 408, 527/540, and 655 nm can be ascribed to the of  ${}^2\text{H}_{9/2} \rightarrow {}^4\text{I}_{15/2}$ ,  ${}^2\text{H}_{11/2}/{}^4\text{S}_{3/2} \rightarrow {}^4\text{I}_{15/2}$ , and  ${}^4\text{F}_{9/2} \rightarrow {}^4\text{I}_{15/2}$  transitions of  $\text{Er}^{3+}$ , respectively. Meanwhile, for blue UC emission phosphor, the emission peaks centered at 450, 475, 647, 690 and 722 nm, corresponding to the  ${}^1\text{D}_2 \rightarrow {}^3\text{F}_4$ ,  ${}^1\text{G}_4 \rightarrow {}^3\text{H}_6$ ,  ${}^1\text{G}_4 \rightarrow {}^3\text{F}_4$ ,  ${}^3\text{F}_2 \rightarrow {}^3\text{H}_6$ , and  ${}^3\text{F}_3 \rightarrow {}^3\text{H}_6$  transitions of  $\text{Tm}^{3+}$ , respectively. The chromaticity coordinates and color purity of the phosphors are calculated according to their corresponding UC emission spectra. The color purity of phosphor is an important feature in evaluating its chromaticity property, which can be calculated using the following equation(Zhang et al., 2016):

$$\text{color purity} = \frac{\sqrt{(x - x_i)^2 + (y - y_i)^2}}{\sqrt{(x_d - x_i)^2 + (y_d - y_i)^2}} \times 100\%$$

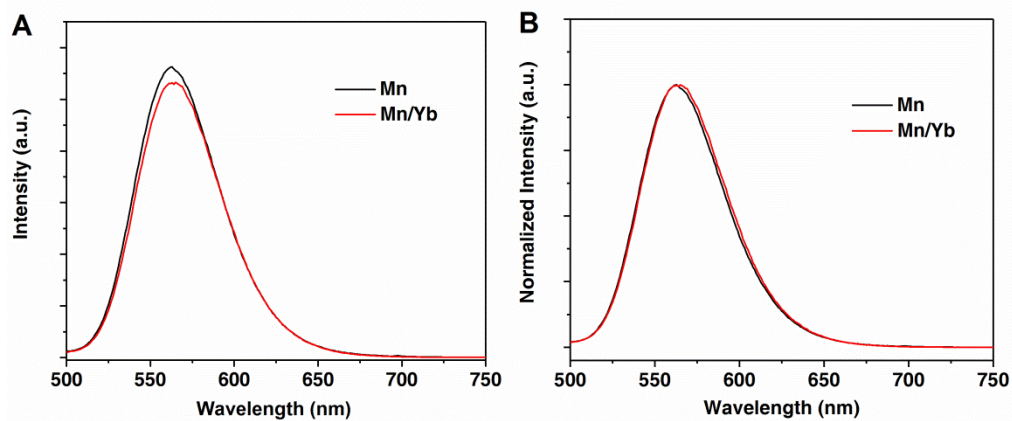
where  $(x, y)$  is the color coordinates of the phosphor,  $(x_i, y_i)$  is the CIE of an equal-energy illuminant with a value of (0.333, 0.333), and  $(x_d, y_d)$  is the chromaticity coordinates corresponding to the dominant wavelength of the light source.



**Figure S4. Temperature dependent UC emission of RCF:0.10Mn<sup>2+</sup>,0.05Yb<sup>3+</sup>, related to Figure 1. (A) Temperature dependent UC emission spectra and (B) the corresponding emission peak position and intensity, and (C) UC luminescence decay curves of RCF:0.10Mn<sup>2+</sup>,0.05Yb<sup>3+</sup> at the temperatures of 77 – 300 K.**

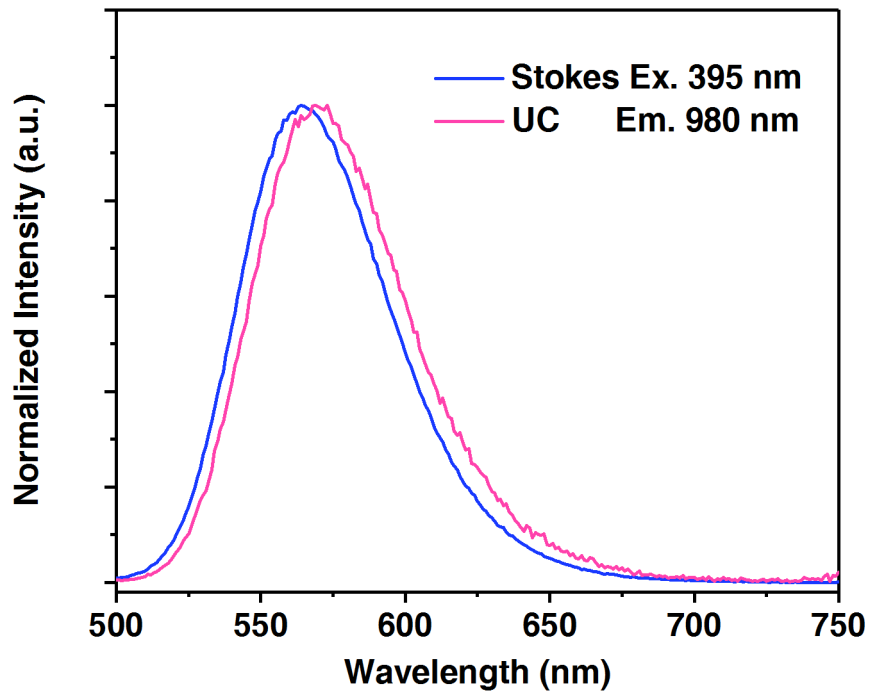


**Figure S5.** UC emission spectra, related to Figure 2. Room temperature UC emission spectra of RCF:0.02Mn<sup>2+</sup>,0.05Yb<sup>3+</sup> (Yb/Mn) and RCF:0.05Yb<sup>3+</sup>,0.03Eu<sup>3+</sup>(Yb/Eu) upon 980 nm laser excitation.

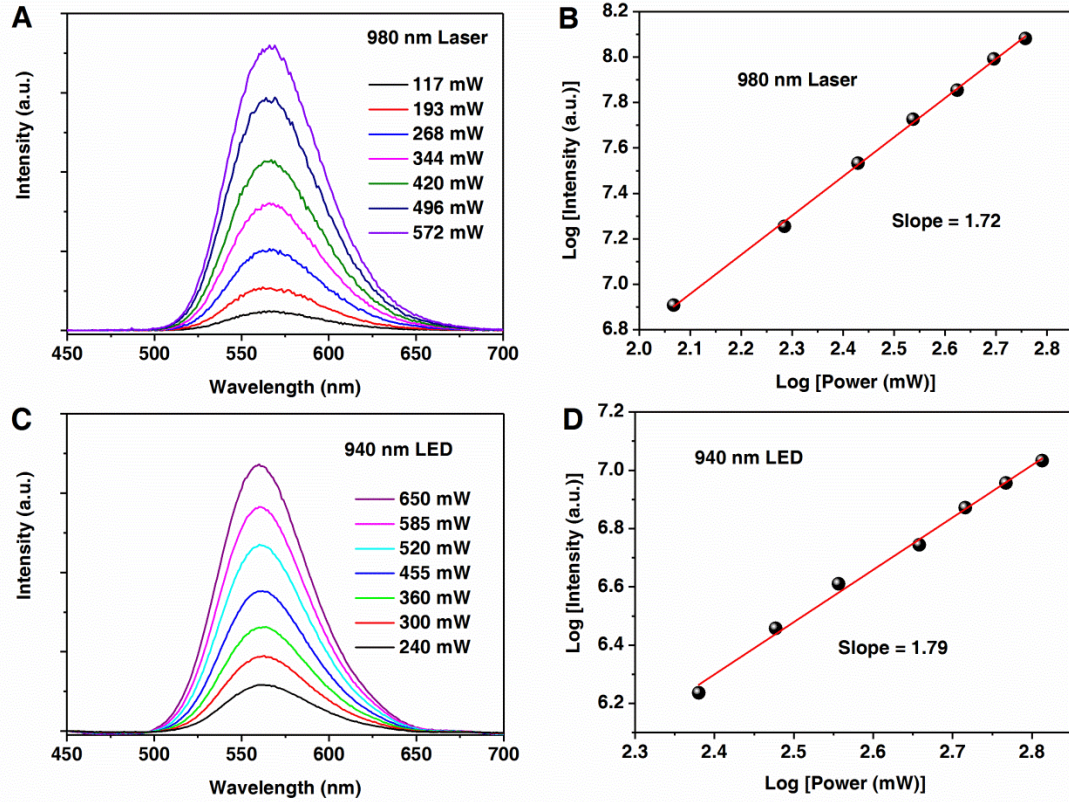


**Figure S6. Room temperature Stokes emission spectra of RCF:0.10Mn<sup>2+</sup> and RCF:0.10Mn<sup>2+</sup>,0.05Yb<sup>3+</sup>, related to Figure 2. Room temperature (A) Stokes emission spectra and (B) the corresponding normalized emission spectra of RCF:0.10Mn<sup>2+</sup> and RCF:0.10Mn<sup>2+</sup>,0.05Yb<sup>3+</sup> upon 395 nm excitation.**

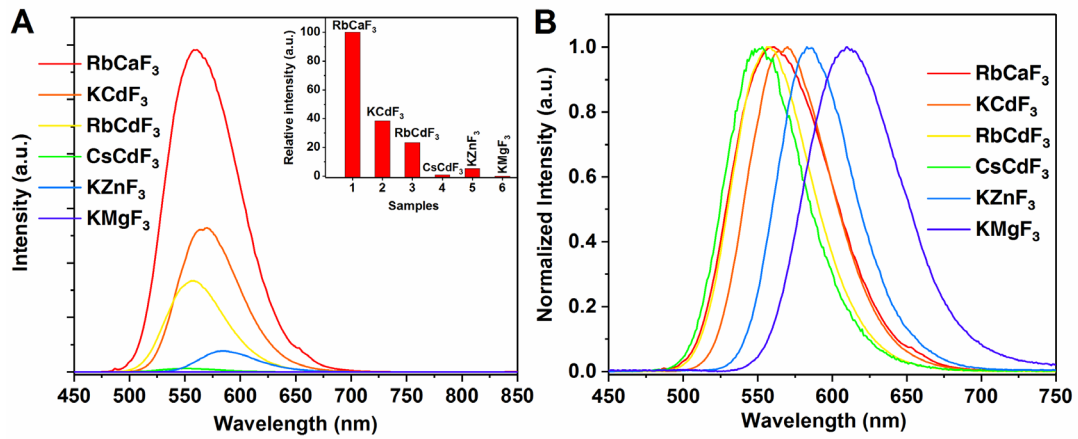




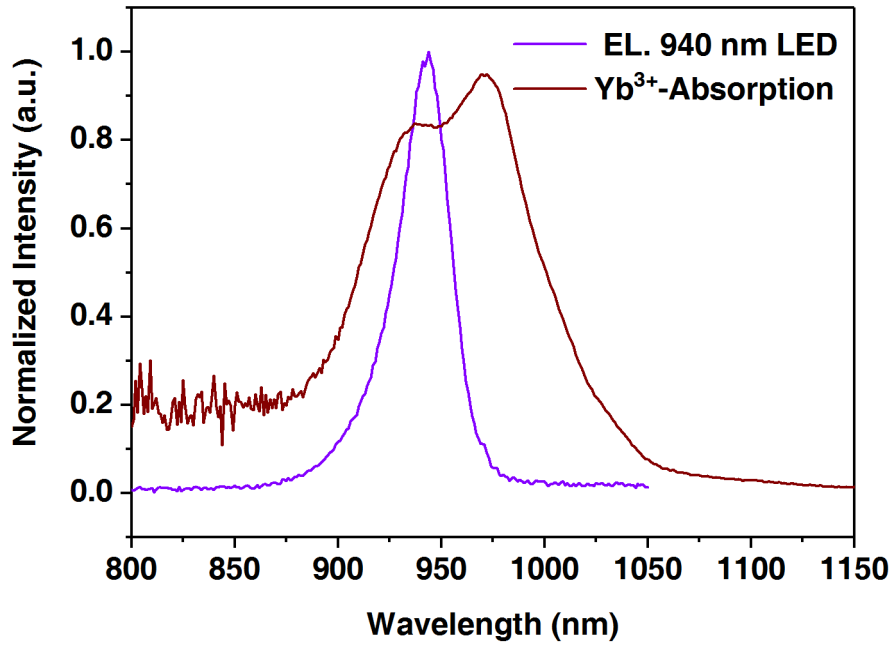
**Figure S7. Stokes emission and UC emission spectra of RCF:0.10Mn<sup>2+</sup>, 0.05Yb<sup>3+</sup>, related to Figure 2. Room temperature Stokes (Ex. 395 nm) and UC (Ex. 980 nm laser) emission spectra of RCF:0.10Mn<sup>2+</sup>, 0.05Yb<sup>3+</sup> under the same measure conditions.**



**Figure S8. Pump-power dependent UC emission of RCF:0.10Mn<sup>2+</sup>,0.05Yb<sup>3+</sup>, related to Figure 1 and Figure 2.** UC emission spectra of RCF:0.10Mn<sup>2+</sup>,0.05Yb<sup>3+</sup> upon excitation of (A) a 980 nm laser diode with a power of 117-572 mW or (C) a 940 nm LED with a power of 240-650 mW. The 980 nm laser (B) and 940 nm LED (D) power dependence of the Mn<sup>2+</sup> UC emissions in RCF:0.10Mn<sup>2+</sup>,0.05Yb<sup>3+</sup>. The slope values are 1.72 and 1.79 for 980 nm laser and 940 nm LED excitation, respectively, indicating the Mn<sup>2+</sup> UC emission belongs to a two-photon processes(Pollnau et al., 2000).



**Figure S9.** UC emission spectra of  $AX_{1-x-y}F_3:xMn^{2+},yYb^{3+}$ , related to **Figure 2**. Room temperature (A) UC emission spectra and (B) Normalized UC emission spectra of  $AX_{1-x-y}F_3:xMn^{2+},yYb^{3+}$  ( $A = Cs, Rb, K; X = Mg, Zn, Cd, Ca$ ) upon 980 nm laser excitation under the same measurements conditions. The inset shows the integrated UC emission intensity of UC materials shown in **Figure S9A**. Except for  $RbCaF_3:xMn^{2+},yYb^{3+}$  ( $x = 0.10, y = 0.05$ ), the optimal doping concentrations of  $Mn^{2+}$  and  $Yb^{3+}$  in other systems are  $x = 0.05, y = 0.02$ , respectively. Except for the  $RbCaF:Mn^{2+},Yb^{3+}$ , all samples are synthesized by a solvothermal method based on the reference ([Song et al., 2016](#)).



**Figure S10. Electroluminescence (EL) spectrum and absorption, related to Figure 1.**

Electroluminescence (EL) spectrum of a 940 nm LED, and near infrared absorption of RCF:0.10Mn<sup>2+</sup>,0.05Yb<sup>3+</sup>.

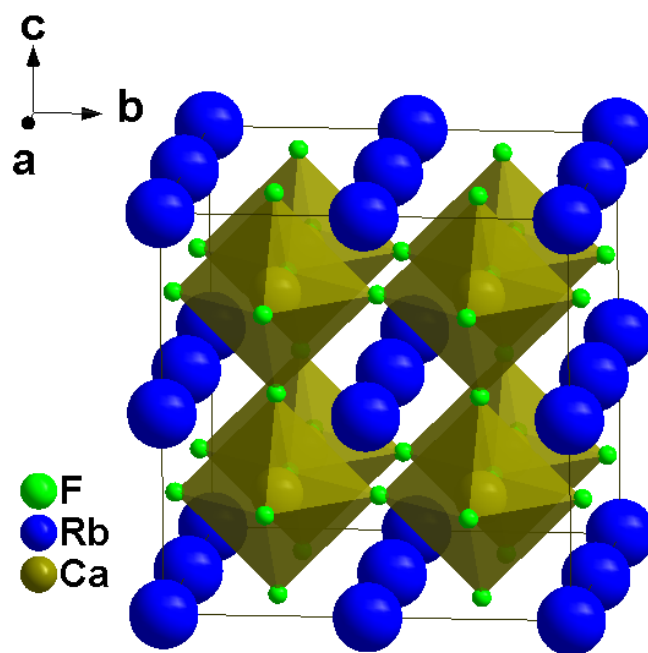
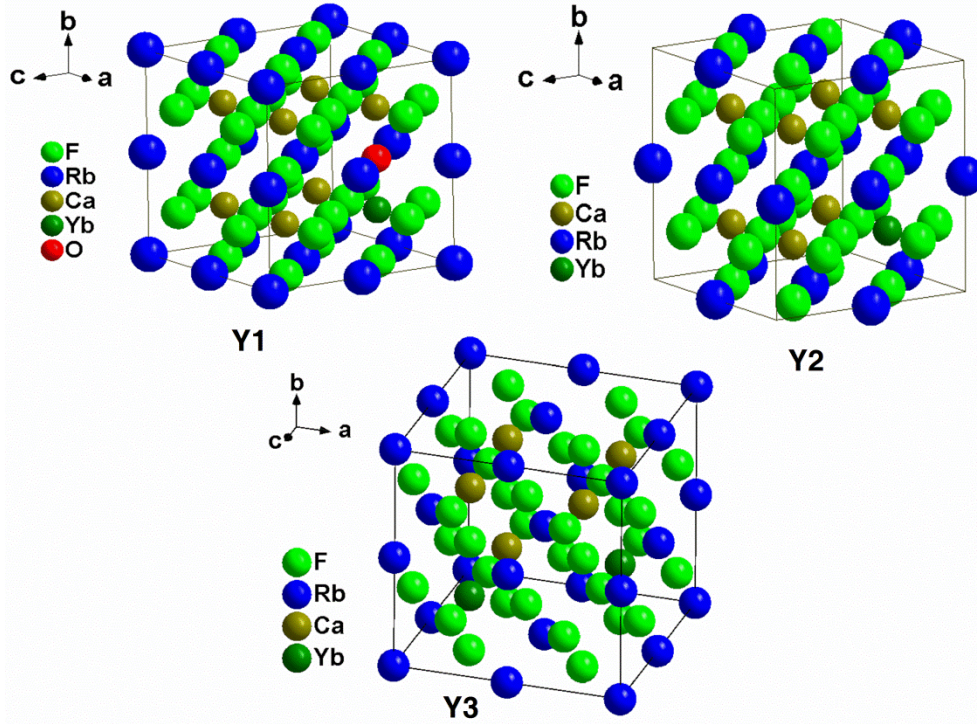
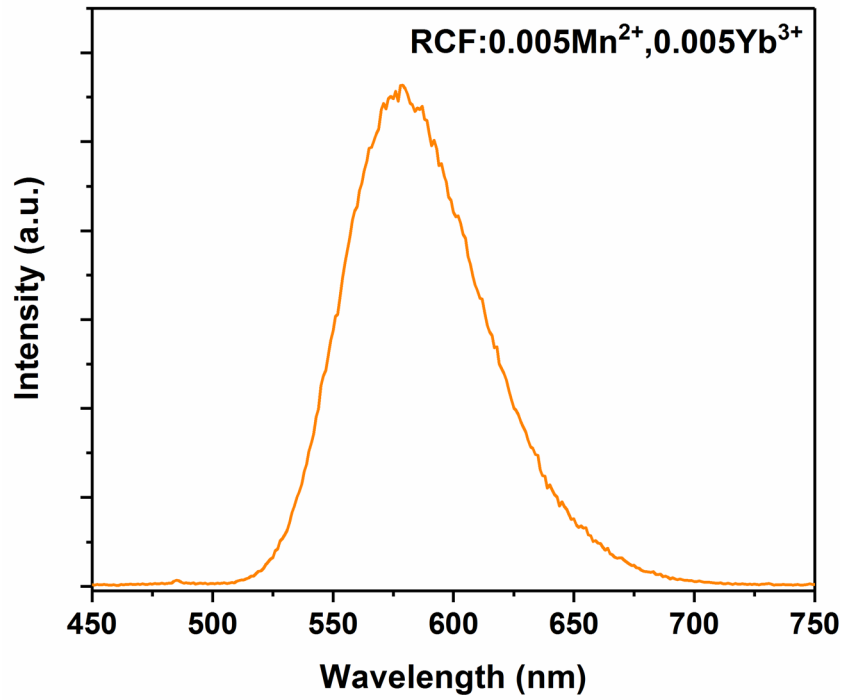


Figure S11. Crystal structure, related to Figure 3. Crystal structure of perovskite  $\text{RbCaF}_3$ .



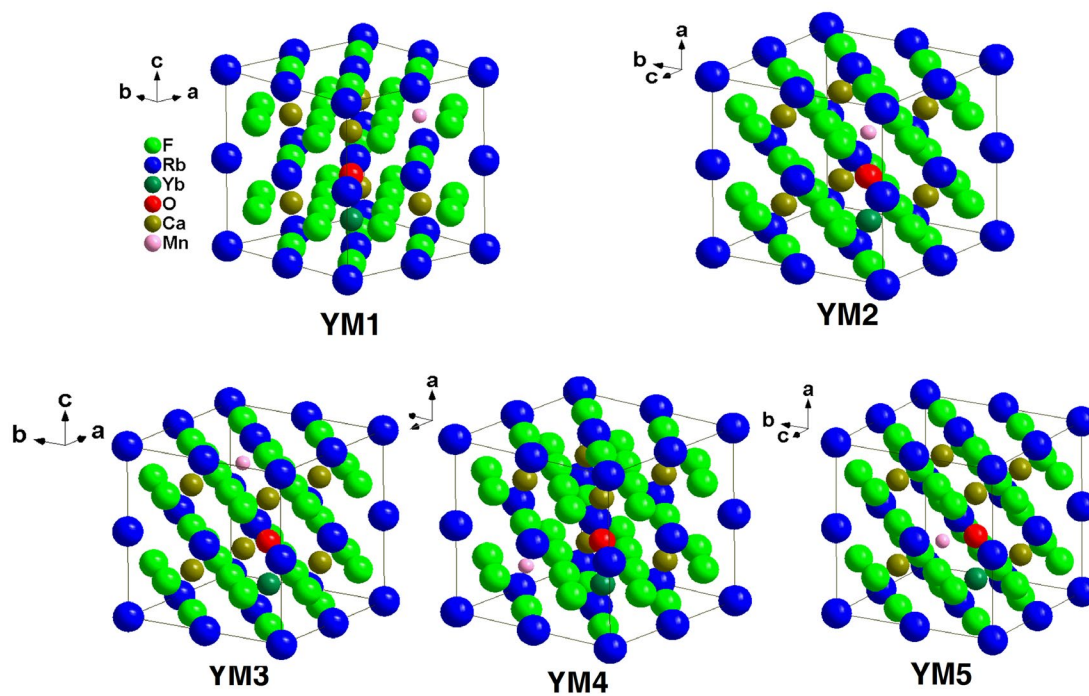


**Figure S12. Different charge compensation models (Y1-Y3) of Yb<sup>3+</sup> substituting Ca<sup>2+</sup> in a 2×2×2 supercell of RCF:Yb<sup>3+</sup>, related to Figure 3.** Y1 and Y2 represent that Yb<sup>3+</sup> occupies Ca<sup>2+</sup> site and produces one oxygen defect (O<sub>F</sub><sup>'</sup>) or Rb<sup>+</sup> vacancy (V<sub>Rb</sub><sup>'</sup>) for charge compensation. The Y<sub>3</sub> represents that two Yb<sup>3+</sup> substitute for two Ca<sup>2+</sup> and simultaneously generates one Ca<sup>2+</sup> vacancy (V<sub>Ca</sub><sup>''</sup>) for charge compensation.

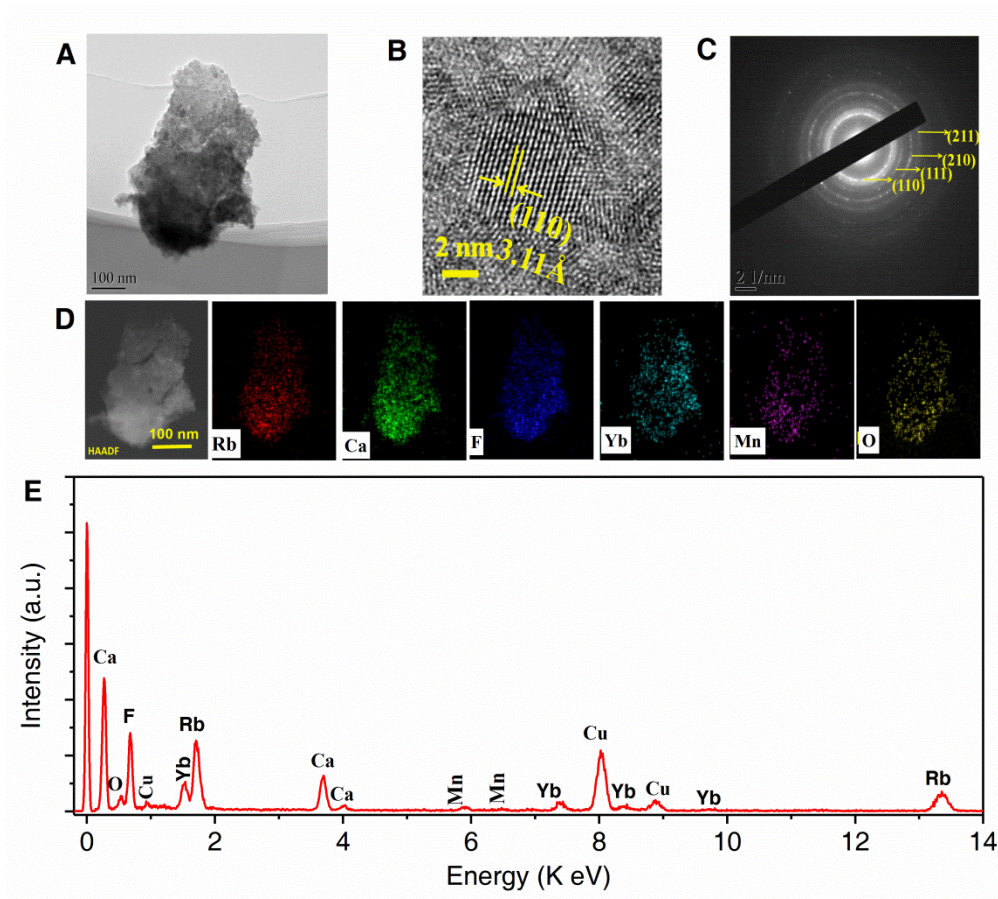


**Figure S13. UC emission spectrum of RCF:0.005Mn<sup>2+</sup>,0.005Yb<sup>3+</sup>, related to Figure 3.**

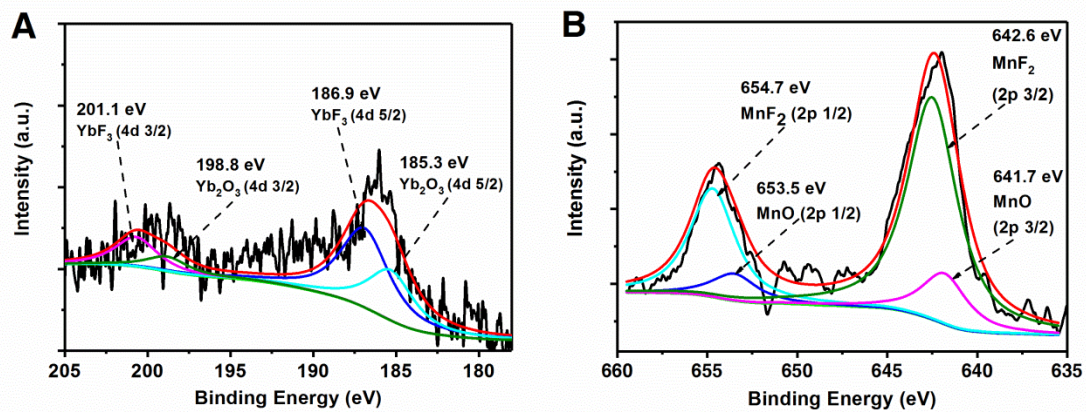
Room temperature UC emission spectrum of RCF:0.005Mn<sup>2+</sup>,0.005Yb<sup>3+</sup> under 980 nm laser excitation.



**Figure S14.** Possible substitution models of  $\text{Yb}^{3+}\text{-O}^{2-}\text{-Mn}^{2+}$  in a  $2 \times 2 \times 2$  supercell  $\text{RCF}:\text{Mn}^{2+}, \text{Yb}^{3+}, \text{O}^{2-}$ , related to Figure 3. Herein, the site substitutions of  $\text{Yb}^{3+}$  and  $\text{O}^{2-}$  are fixed. There five different substitution models (YM1, YM2, YM3, YM4 and YM5).



**Figure S15.** TEM and EDS of RCF:0.10Mn<sup>2+</sup>,0.05Yb<sup>3+</sup>, related to Figure 3. (A) TEM micrograph, (B) high resolution TEM image and (C) selected area electron diffraction (SAED) pattern of RCF:0.10Mn<sup>2+</sup>,0.05Yb<sup>3+</sup>. (D) HAADF-STEM and the element mapping distribution of the elements in RCF:0.10Mn<sup>2+</sup>,0.05Yb<sup>3+</sup>, and (E) the energy dispersive spectrum (EDS) of this sample.



**Figure S16. High-resolution XPS of Yb<sup>3+</sup>(4d) and Mn<sup>2+</sup>(2p) in RCF:0.10Mn<sup>2+</sup>,0.05Yb<sup>3+</sup>, related to Figure 3. High-resolution XPS of Yb<sup>3+</sup>(4d) (A) and Mn<sup>2+</sup>(2p) (B) in RCF:0.10Mn<sup>2+</sup>,0.05Yb<sup>3+</sup>. The Yb-F, Yb-O, Mn-F and Mn-O bonds have been observed in RCF:0.10Mn<sup>2+</sup>,0.05Yb<sup>3+</sup> and the Mn-F and Yb-F bonds were predominant.**



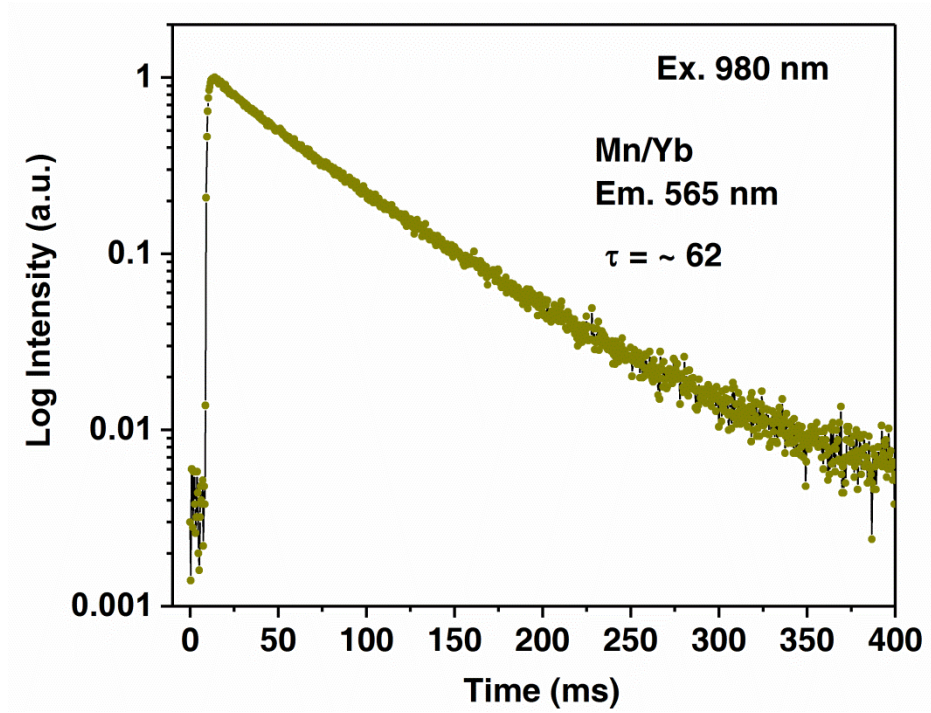
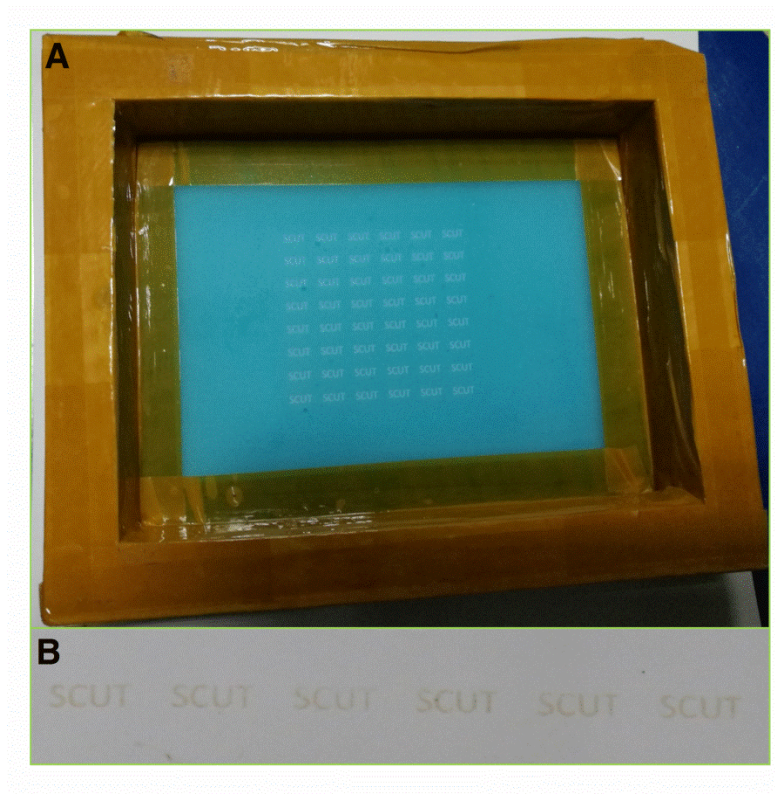
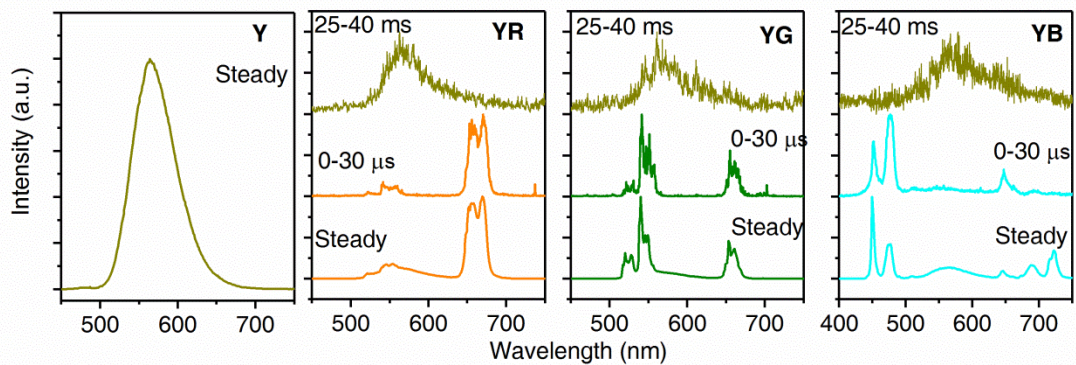


Figure S17. Luminescence decay curve of RCF:0.10Mn<sup>2+</sup>,0.05Yb<sup>3+</sup> (Mn/Yb), related to Figure 3. Room temperature luminescence decay curve of RCF:0.10Mn<sup>2+</sup>,0.05Yb<sup>3+</sup> (Mn/Yb).

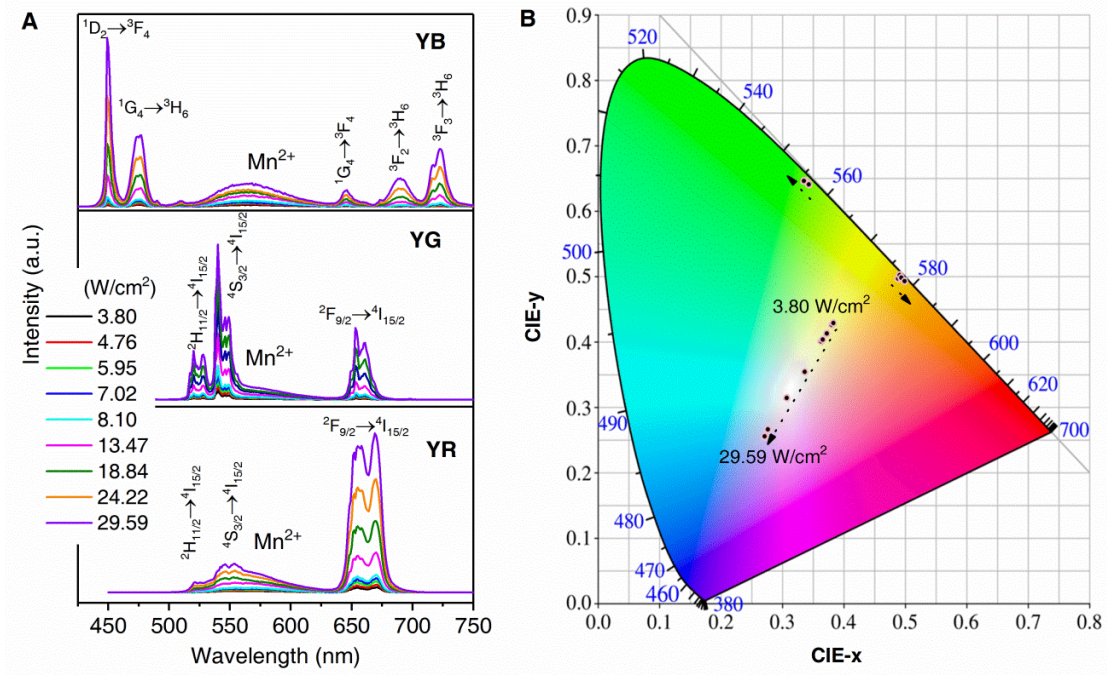




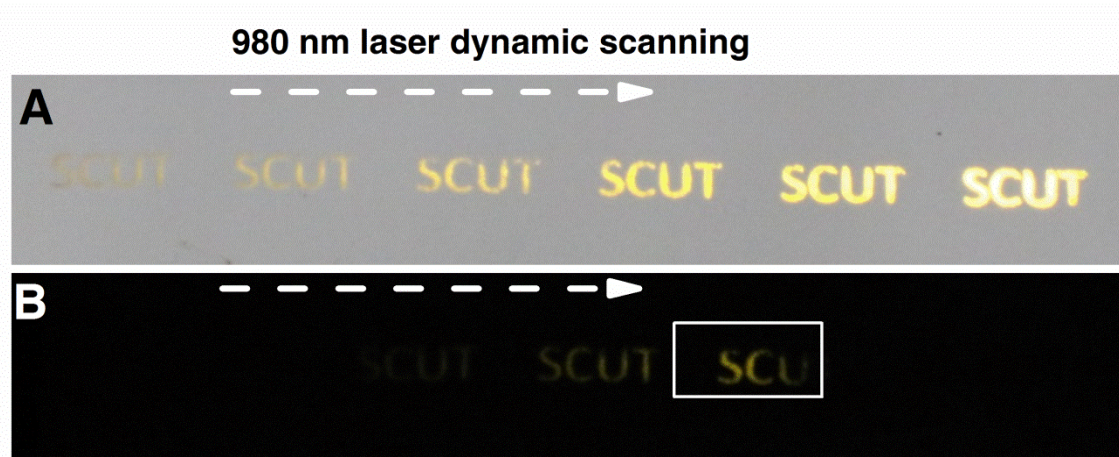
**Figure S18.** The designed “SCUT” screen stencil and the printed pattern “SCUT”, related to **Figure 4**. The designed “SCUT” screen stencil and **(B)** the printed pattern “SCUT” on the paper via screen printing. The “SCUT” on the paper seems to a little yellowy, which corresponds to the body color of the used commercial blank ink.



**Figure S19. Steady and time resolved UC emission spectra of RCF:0.10Mn<sup>2+</sup>,0.05Yb<sup>3+</sup> (Y) and inks YR, YG and YB, related to Figure 4.** Time resolved UC emission spectra of inks YR, YG and YB were obtained by using 7 ns pulse laser excitation. In steady UC emission spectra, both the broad band emission of RCF:0.10Mn<sup>2+</sup>,Yb<sup>3+</sup> and the sharp line emissions of commercial UC phosphors can be observed in YR, YG and YB inks. While, in the times of 0-30  $\mu$ s, only the sharp line like emission from Er<sup>3+</sup>(YR, YG) and Tm<sup>3+</sup> (YB) can be observed, due to the luminescence rise time of RCF:0.10Mn<sup>2+</sup>,Yb<sup>3+</sup> is much longer than that of other inks, the latter would faster get their steady UC luminescence. Meanwhile, during the time of 25-40 ms, only a similar UC emission spectrum of RCF:0.10Mn<sup>2+</sup>,Yb<sup>3+</sup> was observed.

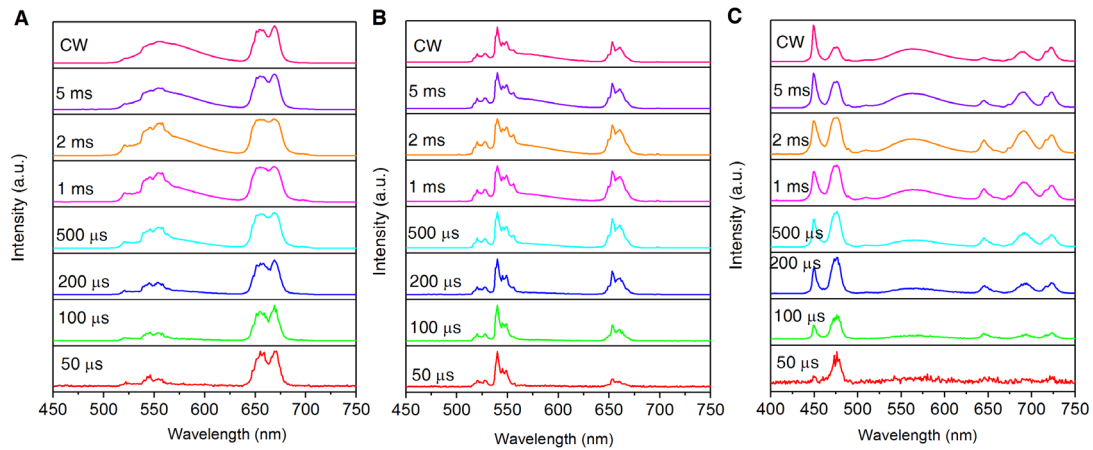


**Figure S20. Pump-power dependent UC emission spectra and CIE coordinates of the designed patterns, related to Figure 4. (A)** UC emission spectra and **(B)** the corresponding chromaticity coordinates of the patterns “SCUT” printed by YR, YG and YB ink, respectively, upon excitation of 980 nm steady laser with a power density from 3.80 to 29.59 W/cm<sup>2</sup>. The emission color of the “SCUT” printed by YB ink shows greatly changed with the increases power density of the laser from 3.80 to 29.59 W/cm<sup>2</sup>, whereas the emission color of the “SCUT” printed by other inks varied small. The significant different power dependent changing trends of the “SCUT” emission color printed by YB ink and other inks can be ascribed to the four and three photons UC processes for the 450 and 475 nm blue emissions (YB), respectively, while two photon UC processes for the 527/540/667 nm in Er<sup>3+</sup> and 565 nm in Mn<sup>2+</sup> emissions.



**Figure S21. Luminescence photographs of the “SCUT” pattern upon 980 nm laser fast scanning, related to Figure 4.** Luminescence photographs of the “SCUT” pattern upon 980 nm laser fast scanning under the (A) daylight environment or (B) dark environment. The power densities of the 980 nm laser are  $29.59 \text{ W/cm}^2$  (A) and  $2.72 \text{ W/cm}^2$  (B), respectively. The highlighted part with white border is laser radiation position.





**Figure S22. Pulse width dependent UC emission spectra of the designed “SCUT” patterns, related to Figure 4.** UC emission spectra of the patterns “SCUT” printed by (A)YR, (B)YG and (C) YB inks upon 980 nm pulse laser excitation with a pulse width from CW to 50  $\mu\text{s}$ . With the decreases the pulse width of the laser, the relative emission intensity of  $\text{Mn}^{2+}$  emission to that of  $\text{Er}^{3+}$  (A, B) or  $\text{Tm}^{3+}$  (c) is monotonously reduced. Particularly, when the pulse width is reduced to 50  $\mu\text{s}$ , the  $\text{Mn}^{2+}$  emission seems almost fully suppressed, only the  $\text{Er}^{3+}$  (A, B) or  $\text{Tm}^{3+}$  (C) UC emissions can be observed. Accordingly, the emission color of the patterns “SCUT” printed by YR, YG and RB ink are changed from orange to red, yellow-green to green, and white to blue, respectively. This phenomenon can be attributed to the non-steady-state absorption time (slow ESA processes for  $\text{Yb}^{3+}\text{-Mn}^{2+}$  pair) for  $\text{Mn}^{2+}$  UC emission is obvious longer than that of  $\text{Yb}^{3+}/\text{Er}^{3+}$  or  $\text{Yb}^{3+}/\text{Tm}^{3+}$  codoped UC phosphors.

## Supplemental Tables

**Table S1. UC emission lifetimes of some Yb<sup>3+</sup>/Mn<sup>2+</sup> based UC systems, related to Figure**

**1.** UC emission lifetimes of some Yb<sup>3+</sup>/Mn<sup>2+</sup> based UC systems reported in previous references. The RT represents the Room temperature.

UC system	Temperature	Wavelength	UC lifetime	Reference
RbMnCl <sub>3</sub> :Yb <sup>3+</sup>	15 K	15750 cm <sup>-1</sup>	1.06 ms	(Valiente et al., 2001)
CsMnBr <sub>3</sub> :Yb <sup>3+</sup>	12 K	14700 cm <sup>-1</sup>	337 μs	(Gerner et al., 2001)
Rb <sub>2</sub> MnCl <sub>4</sub> :Yb <sup>3+</sup>	15 K	16200 cm <sup>-1</sup>	9.7 ms	(Reinhard et al., 2002)
Zn <sub>2</sub> SiO <sub>4</sub> :Mn <sup>2+</sup> ,Yb <sup>3+</sup>	12 K	19050 cm <sup>-1</sup>	τ <sub>fast</sub> = 400 μs τ <sub>slow</sub> = 1.2 ms	(Gerner et al., 2004)
LaMgAl <sub>11</sub> O <sub>19</sub> :Mn <sup>2+</sup> ,Yb <sup>3+</sup>	RT	514 nm	5.8 ms	(Martín-Rodríguez et al., 2009)
NaGdF <sub>4</sub> :Yb/Tm@NaGdF <sub>4</sub> :Mn	RT	535 nm	30 ms	(Li et al., 2015)
KMgF <sub>3</sub> : Mn <sup>2+</sup> ,Yb <sup>3+</sup>	RT	610 nm	25.56 ms	(Song et al., 2016)
KZnF <sub>3</sub> : Mn <sup>2+</sup> ,Yb <sup>3+</sup>		585 nm	43.38 ms	
KCdF <sub>3</sub> : Mn <sup>2+</sup> ,Yb <sup>3+</sup>		567 nm	30.72ms	
RbCdF <sub>3</sub> : Mn <sup>2+</sup> ,Yb <sup>3+</sup>		563 nm	46.72ms	
CsCdF <sub>3</sub> : Mn <sup>2+</sup> ,Yb <sup>3+</sup>		550 nm	24.96ms	
RbCaF <sub>3</sub> : Mn <sup>2+</sup> ,Yb <sup>3+</sup>	77 K	587 nm	138 ms	This work
RbCaF <sub>3</sub> : Mn <sup>2+</sup> ,Yb <sup>3+</sup>	RT	565 nm	62 ms	This work
CaO:Mn <sup>2+</sup> ,Yb <sup>3+</sup>	RT	600 nm	10.87 ms	(Wang et al., 2016)
NaGdF <sub>4</sub> :Mn@NaGdF <sub>4</sub> :Yb/Tm@NaYF <sub>4</sub>	RT	550 nm	39 ms	(Liu et al., 2017)

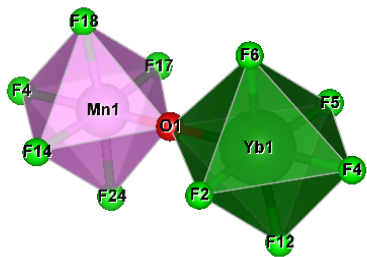

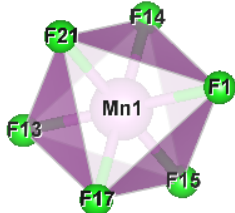


**Table S2. Absolute quantum yield, related to Figure 1.** Absolute quantum yield of UC emission of RCF:0.10Mn<sup>2+</sup>,0.05Yb<sup>3+</sup> upon 980 nm laser excitation.

Sample	Power density (W/cm <sup>2</sup> )	Quantum yield (%)
RCF:0.10Mn <sup>2+</sup> ,0.05Yb <sup>3+</sup>	50	0.015
	80	0.016
	150	0.021

The absolute UC emission quantum yield (QY) of the samples was measured by using a standard barium sulfate coated integrating sphere (150 mm in diameter, Edinburgh) as the sample chamber, and that was mounted on the FLS920 spectrometer with the entry and output port of the sphere located in 90° geometry from each other in the plane of the spectrometer(Zheng et al., 2018).

**Table S3. The typical parameters of the polyhedron, related to Figure 3.** The coordination environment, bonds distances, and polyhedron distortion index of  $\text{Mn}^{2+}$  or  $\text{Yb}^{3+}$  in the  $2 \times 2 \times 2$  super cell of  $\text{RbCaF}_3:\text{Mn}^{2+}, \text{Yb}^{3+}$  (I),  $\text{RbCaF}_3:\text{Yb}^{3+}$  (II) and  $\text{RbCaF}_3:\text{Mn}^{2+}$  (III) after structure optimization.

Coordination environment of $\text{Mn}^{2+}$ or $\text{Yb}^{3+}$	Bonds distance (Å)	Polyhedron distortion index
 <p style="text-align: center;"><b>I</b></p>	(Mn1-F4)=2.13357	0.03739
	(Mn1-F14)=2.00288	
	(Mn1-O1)=1.76190	
	(Mn1-F17)=2.00288	
	(Mn1-F18)=2.00288	
	(Mn1-F24)=2.00288	
	Mn-F=1.9845*	
	(Yb1-F2)=2.14651	0.04685
	(Yb1-F5)=2.14651	
	(Yb1-F6)=2.14651	
	(Yb1-F4)=2.46039	
	(Yb1-F12)=2.14651	
	(Yb1-O1)=2.30170	
	Yb-F=2.22470*	
 <p style="text-align: center;"><b>II</b></p>	(Yb1-F1)=2.16498	0.00597
	(Yb1-F13)=2.16498	
	(Yb1-F14)=2.16498	
	(Yb1-F15)=2.13840	
	(Yb1-F17)=2.16498	
	(Yb1-O1)=2.20625	
	Yb-F=2.16740*	
 <p style="text-align: center;"><b>III</b></p>	(Mn1-F1)=2.03530	0.00000
	(Mn1-F13)=2.03530	
	(Mn1-F14)=2.03530	
	(Mn1-F15)=2.03530	
	(Mn1-F17)=2.03530	
	(Mn1-F21)=2.03530	
	Mn-F=2.03530*	

\*Means average bond-distance. All the above data are obtained based on the optimized structures by using the software VESTA. It is found that the formation of  $\{\text{Yb}^{3+}-\text{O}^{2-}-\text{Mn}^{2+}\}$  unit ( $\text{Yb}^{3+}-\text{Mn}^{2+}$  pair) would cause obvious crystal field environment distortion of the  $\text{Mn}^{2+}$  and  $\text{Yb}^{3+}$  in  $\text{RbCaF}_3:\text{Mn}^{2+}, \text{Yb}^{3+}$ .

**Table S4. The designed security inks, related to Figure 4.** The security inks (Y, YR, YG and YB) are made based on the as-synthesized yellow UC phosphor RCF: 0.10Mn<sup>2+</sup>,0.05Yb<sup>3+</sup> (Y), commercial red (R,  $\beta$ -NaYbF<sub>4</sub>:6%Er<sup>3+</sup>), or green (G,  $\beta$ -NaYF<sub>4</sub>:20%Yb<sup>3+</sup>,2%Er<sup>3+</sup>) or blue (B,  $\beta$ -NaYF<sub>4</sub>:20%Yb<sup>3+</sup>,2%Tm<sup>3+</sup>) UC phosphor, and commercial blank ink.

Inks	Y(g)	R(g)	G(g)	B(g)	Commercial blank ink (g)
Y	0.30	-	-	-	1.0
YR	0.3	0.042	-	-	1.0
YG	0.3	-	0.003	-	1.0
YB	0.3	-	-	0.03	1.0

**Table S5. The chromaticity coordinates of the designed patterns, related to Figure 4.** The chromaticity coordinates of the patterns “SCUT” printed by YR, YG and YB ink upon steady 980 nm laser excitation with a power density of 3.80-29.59 W/cm<sup>2</sup>.

<b>Power density (W/cm<sup>2</sup>)</b>	<b>YR CIE (x, y)</b>	<b>YG CIE (x, y)</b>	<b>YB CIE (x, y)</b>
3.80	0.4882, 0.5033	0.3424, 0.6411	0.3794, 0.4262
4.76	0.4927, 0.4993	0.3408, 0.6436	0.3830, 0.4290
5.95	0.4882, 0.5046	0.3427, 0.6420	0.3717, 0.4135
7.02	0.4877, 0.5055	0.3424, 0.6424	0.3621, 0.4014
8.10	0.4903, 0.5030	0.3404, 0.6443	0.3650, 0.4046
13.47	0.4905, 0.5031	0.3368, 0.6473	0.3357, 0.3545
18.47	0.4939, 0.4991	0.3371, 0.6467	0.3070, 0.3151
24.22	0.4979, 0.4951	0.3320, 0.6508	0.2764, 0.2673
29.59	0.4992, 0.4934	0.3355, 0.6471	0.2713, 0.2560

## Transparent Methods

**Materials and Synthesis:** The reagents in this work were Yb<sub>2</sub>O<sub>3</sub> (99.998%), CaF<sub>2</sub> (99.99%), MnCO<sub>3</sub> (99%), NH<sub>4</sub>HF<sub>2</sub> (99.99%), RbF (99.9%). Yb<sub>2</sub>O<sub>3</sub> was supplied by Alfa Aesar Reagent Company (Shanghai, China), and the other chemicals were purchased from Aladdin Industrial Corporation (Shanghai, China). All of the chemicals were used as received without further purification. A series of RbCa<sub>(1-x-y)</sub>F<sub>3</sub>:xMn<sup>2+</sup>,yYb<sup>3+</sup> (0 ≤ x ≤ 0.20; y = 0, 0.05) samples were synthesised by a traditional solid-state reaction method. The raw materials of RbF, CaF<sub>2</sub>, MnCO<sub>3</sub>, Yb<sub>2</sub>O<sub>3</sub> and NH<sub>4</sub>HF<sub>2</sub> were weighed and mixed homogeneously in an agate mortar in a glove box. The mixture was first preheated at 200 °C under argon gas protection for 2.5 h and then sintered at 850 °C for 4 h. As the systems were cooled to room temperature in the furnace, the products were collected and reground for further characterization.

**Characterization:** The phase and crystal structure of the samples were determined using an X-ray diffractometer (Philips Model PW1830) with Cu-Kα radiation (λ=1.5406 Å). The morphology and energy dispersive x-ray spectroscopy characterizations were performed using SEM (Nova, NANO SEM 430) and TEM (JEOL, 2100F), respectively. The X-ray photoelectron spectroscopy (XPS) was performed by ESCALAB250Xi (Thermo Scientific, USA). The excitation/emission spectra and luminescence decay curves were recorded using an FLS920 fluorescence spectrophotometer (Edinburgh Instrument) equipped with both continuous and microsecond flash Xenon (Xe) lamp as excitation sources. Furthermore, the UC emission spectra were measured by a Jobin-Yvon Triax 320 spectrofluorometer equipped with a R928 photomultiplier tube (PMT) in conjunction with a 980-nm diode laser with both continuous and pulsed modes. The absorption spectrum of the sample was collected by an UV2600 Spectrophotometer (SHIMADZU).

The time-resolved PL spectra and the of samples were measured by using an output at a central wavelength of 980 nm with pulse duration of 7 ns and a varied repetition rate from

single shot to 20 Hz as the excitation source (Opolette 355 LD). The laser beam was focused onto the samples using a lens with a focus length of 100 mm. To minimize the scattering, the emission was collected at the direction perpendicular to the excitation. The emission signal was directed into a monochromator with two exit ports (Andor, SR-500I). One port is integrated with ICCD (Andor, DH320T-18U-63) with a minimum gate width of 2 ns for time resolved spectra measurement. The other port is mounted with a photon counting detector combined with the multichannel scaler/average (SR430) for single wavelength PL lifetime measurement. An 850 nm short pass filter was placed before the spectrometer to minimize the scattering from the excitation light. The low temperature dependent UC emission spectra and luminescence decay curves were measured using an Edinburgh FLS980 spectrometer equipped with a CTI-Cryogenics temperature controlling system, and the excitation source is a 980 nm diode laser with both continuous and pulsed modes.

**Theoretical calculations:** Theoretical calculations were performed by using density functional theory (DFT) implemented in the Vienna *ab initio* simulation package (Vasp) (Kresse and Joubert, 1999; Kresse and Furthmüller, 1996). The exchange correlation potential was approximated by generalized gradient approximation (GGA) with the PBE functional (Perdew et al., 1996). The cutoff energy  $E_{cut}$  and k-point mesh were set to 400 eV and the 2×2×2 Monkhorst-Pack grid, respectively, which are sufficient for energy convergence. The convergence criterion for the electronic energy was  $10^{-5}$  eV and the structures were relaxed until the Hellmann–Feynman forces were smaller than  $0.02$  eV Å<sup>-1</sup>. The formation energy ( $E_f$ ) of the Mn<sup>2+</sup>, Yb<sup>3+</sup>doped RbCaF<sub>3</sub> can be calculated by (Wei and Zhang, 2002):

$$E_f = E(doped) - E(perfect) - \sum n_i \mu_i \quad (5)$$

where  $E(doped)$  and  $E(perfect)$  are the total energy of the doped and perfect (undoped) crystal, respectively. The  $\mu_i$  and  $n_i$  represent the chemical potential and the number of the added ( $n_i > 0$ ) or removed ( $n_i < 0$ ) i-type atoms, respectively.



**LED performances:** UC luminescence LED was fabricated based on the commercial 940-nm AlGaAs near infrared emission chip (40 mil  $\times$  40 mil, TK0H40IRA) and UC luminescence phosphor RbCaF<sub>3</sub>:Mn<sup>2+</sup>,Yb<sup>3+</sup>, and the packing procedure is similar to that of the common phosphor converted white LEDs. The UC emission spectra of the above UC luminescence LED were detected by a FLS920 fluorescence spectrophotometer (Edinburgh Intrument), and a direct current (DC) power system to control the ouput power of the UC luminescence LED.

**Information encryption and anti-counterfeiting performances:**The security inks were made by mixing the synthesized UC luminescence RbCaF<sub>3</sub>:Mn<sup>2+</sup>,Yb<sup>3+</sup> and/or commercial RGB (Red, Green, Blue) UC luminescence phosphors (purchased from SHENZHEN CITY NINGJING ZHIYUAN ANTI FALSE PIGMENT TECHONOLOGY CO., LTD, China) with commercial blank screen printing ink (SND-100, purchased from ZHONGYI INK & PAINT CO., LTD, China). Different performances of luminescent ink can be obtained by controlling the mass ratio of the as-synthesized UC luminescence phosphor RbCaF<sub>3</sub>:Yb<sup>3+</sup>,Mn<sup>2+</sup> to the RGB commercial UC luminescence phosphor. Using the above luminescent inks, a series of designed patterns were printed on paper or Chinese banknote. The luminescence images and demonstration movies were recorded by a camera (Canon, EOS 80D, EF-S 18-200 mm f/3.5-5.6 IS) in an all-manual mode and using a 980 nm laser diode with spot diameter of  $\sim$  3 mm as excitation source. The demonstration videos were recorded using a camera with a frame rate of 50 frame/s. To more clearly display about the color separation of the UC luminescence of RCF:Mn<sup>2+</sup>,Yb<sup>3+</sup> and other lanthanide doped UC materials, the frame rate of the videos (Videos S2-6, Supporting Information) were decreased to 30 frame/s. The dynamic scanning of the laser was realized by fixed the 980 nm laser diode on a homemade automatic control device, and the laser scan speed for the dynamic color separation is about 8.38 cm/s.

## SUPPLEMENTAL REFERENCES:

- Gerner, P., Fuhrer, C., Reinhard, C., and Güdel, H.U. (2004). Near-infrared to visible photon upconversion in  $\text{Mn}^{2+}$  and  $\text{Yb}^{3+}$  containing materials. *J. Alloy Compd.*, *380*, 39-44.
- Gerner, P., Wenger, O.S., Valiente, R., and Güdel, H.U. (2001). Green and Red Light Emission by Upconversion from the near-IR in  $\text{Yb}^{3+}$  Doped  $\text{CsMnBr}_3$ . *Inorg. Chem.*, *40*, 4534-4542.
- Kresse, G., and Furthmüller, J. (1996). Efficient iterative schemes for ab initio total-energy calculations using a plane-wave basis set. *Phys. Rev. B* *54*, 11169.
- Kresse, G., and Joubert, D. (1999). From ultrasoft pseudopotentials to the projector augmented-wave method. *Phys. Rev. B* *59*, 1758.
- Li, X., Liu, X., Chevrier, D.M., Qin, X., Xie, X., Song, S., Zhang, H., Zhang, P., and Liu, X. (2015). Energy migration upconversion in manganese(II)-doped nanoparticles. *Angew. Chem. Int. Ed.*, *54*, 13312-13317.
- Liu, X., Wang, Y., Li, X., Yi, Z., Deng, R., Liang, L., Xie, X., Loong, D.T.B., Song, S., and Fan, D., *et al.* (2017). Binary temporal upconversion codes of  $\text{Mn}^{2+}$ -activated nanoparticles for multilevel anti-counterfeiting. *Nat. Commun.*, *8*, 899.
- Martín-Rodríguez, R., Valiente, R., and Bettinelli, M. (2009). Room-temperature green upconversion luminescence in  $\text{LaMgAl}_{11}\text{O}_{19}:\text{Mn}^{2+},\text{Yb}^{3+}$  upon infrared excitation. *Appl. Phys. Lett.* *95*, 91913.
- Perdew, J.P., Burke, K., and Ernzerhof, M. (1996). Generalized gradient approximation made simple. *Phys. Rev. Lett.* *77*, 3865.
- Pollnau, M., Gamelin, D.R., Lüthi, S.R., Güdel, H.U., and Hehlen, M.P. (2000). Power dependence of upconversion luminescence in lanthanide and transition-metal-ion systems. *Phys. Rev. B* *61*, 3337-3346.
- Reinhard, C., Valiente, R., and Güdel, H.U. (2002). Exchange-induced upconversion in  $\text{Rb}_2\text{MnCl}_4:\text{Yb}^{3+}$ . *J. Phys. Chem. B* *106*, 10051-10057.
- Song, E., Chen, Z., Wu, M., Ding, S., Ye, S., Zhou, S., and Zhang, Q. (2016). Room-temperature wavelength-tunable single band upconversion luminescence from  $\text{Yb}^{3+}/\text{Mn}^{2+}$  codoped fluoride perovskites  $\text{ABF}_3$ . *Adv. Opt. Mater.* *4*, 798-806.
- Valiente, R., Wenger, O.S., and Güdel, H.U. (2001). Near-infrared-to-visible photon upconversion process induced by exchange interactions in  $\text{Yb}^{3+}$ -doped  $\text{RbMnCl}_3$ . *Phys. Rev. B* *63*, 165102.
- Wang, J.L., Song, E.H., Wu, M., Dai, W.B., Jiang, X.F., Zhou, B., and Zhang, Q.Y. (2016). Room-temperature green to orange color-tunable upconversion luminescence from  $\text{Yb}^{3+}/\text{Mn}^{2+}$  co-doped  $\text{CaO}$ . *J Mater. Chem. C* *4*, 1116-1154.
- Wei, S., and Zhang, S.B. (2002). Chemical trends of defect formation and doping limit in II-VI semiconductors: The case of  $\text{CdTe}$ . *Phys. Rev. B* *66*, 155211.

Zhang, X., Tsai, Y., Wu, S., Lin, Y., Lee, J., Sheu, H., Cheng, B., and Liu, R. (2016). Facile atmospheric pressure synthesis of high thermal stability and narrow-band red-emitting SrLiAl<sub>3</sub>N<sub>4</sub>:Eu<sup>2+</sup> index white light-emitting diodes. *ACS Appl. Mater. Interfaces* 8, 19612-19617.

Zheng, W., Huang, P., Gong, Z., Tu, D., Xu, J., Zou, Q., Li, R., You, W., Bünzli, J.G., and Chen, X. (2018). Near-infrared-triggered photon upconversion tuning in all-inorganic cesium lead halide perovskite quantum dots. *Nat, Commun.* 9, 3462.